J. Fluid Mech. (2023), *vol.* 974, A49, doi:10.1017/jfm.2023.803

Direct numerical simulation of a zero-pressure-gradient turbulent boundary layer with passive scalars up to Prandtl number $Pr = 6$

Arivazhagan G. Balasubramanian[1,2,†], **Luca Guastoni**[1,2], **Philipp Schlatter**[1,2,3] and **Ricardo Vinuesa**[1,2,†]

[1]FLOW, Engineering Mechanics, KTH Royal Institute of Technology, Stockholm, Sweden

[2]Swedish e-Science Research Centre (SeRC), Stockholm, Sweden

[3]Institute of Fluid Mechanics, Friedrich-Alexander Universität, Erlangen-Nürnberg, Germany

(Received 30 January 2023; revised 15 July 2023; accepted 16 September 2023)

The objective of the present study is to provide a numerical database of thermal boundary layers and to contribute to the understanding of the dynamics of passive scalars at different Prandtl numbers. In this regard, a direct numerical simulation (DNS) of an incompressible zero-pressure-gradient turbulent boundary layer is performed with the Reynolds number based on momentum thickness Re_θ ranging up to 1080. Four passive scalars, characterized by the Prandtl numbers $Pr = 1, 2, 4, 6$ are simulated using the pseudo-spectral code SIMSON (Chevalier *et al.*, SIMSON : a pseudo-spectral solver for incompressible boundary layer flows. *Tech. Rep.* TRITA-MEK 2007:07. KTH Mechanics, Stockholm, Sweden, 2007). To the best of our knowledge, the present DNS provides the thermal boundary layer with the highest Prandtl number available in the literature. It corresponds to that of water at $\sim$24 °C, when the fluid temperature is considered as a passive scalar. Turbulence statistics for the flow and thermal fields are computed and compared with available numerical simulations at similar Reynolds numbers. The mean flow and scalar profiles, root-mean-squared velocity and scalar fluctuations, turbulent heat flux, turbulent Prandtl number and higher-order statistics agree well with the numerical data reported in the literature. Furthermore, the pre-multiplied two-dimensional spectra of the velocity and of the passive scalars are computed, providing a quantitative description of the energy distribution at the different length scales for various wall-normal locations. The energy distribution of the heat-flux fields at the wall is concentrated on longer temporal structures with increasing Prandtl number. This is due to the thinner thermal boundary layer as thermal diffusivity decreases and, thereby, the longer temporal structures exhibit a different footprint at the wall.

† Email addresses for correspondence: argb@kth.se, rvinuesa@mech.kth.se

Key words: turbulent boundary layers

1. Introduction

Wall-bounded turbulence is a phenomenon of huge technological importance in many industrial and environmental applications. Understanding and predicting the behaviour of turbulent flows are critical in various fields, such as energy production, environmental modelling and fluid-dynamics research. However, investigating turbulent flow in complex geometries poses considerable challenges from both numerical and experimental perspectives. For this reason, simpler geometries are chosen when the fundamental physics of the flow is studied. One canonical flow case widely used in the literature is the boundary layer developing on a flat surface (Spalart 1988; Schlatter *et al.* 2009). The spatially evolving fully turbulent boundary layer has been studied using different experimental techniques (Österlund 1999; Rahgozar, Maciel & Schlatter 2013; Shehzad *et al.* 2021) with researchers constantly improving the measurement techniques (Örlü & Alfredsson 2010; Bailey *et al.* 2013; Vinuesa & Nagib 2016) to obtain reliable measurements at high Reynolds numbers (Samie *et al.* 2018). At the same time, direct numerical investigations of turbulent boundary layers have been performed in several studies (Spalart 1988; Ferrante & Elghobashi 2005; Wu & Moin 2009; Simens *et al.* 2009; Schlatter *et al.* 2010) implementing different solution methods for an increasing range of Reynolds numbers. Given the resolution limitations of experimental techniques in capturing the near-wall region of boundary-layer flow, direct numerical simulations (DNSs) have emerged as a valuable tool for investigating the transport phenomena in turbulence (Araya & Castillo 2012). However, the applicability of DNS is currently constrained to low-Reynolds-number flows due to its significant computational costs. Despite this limitation, DNS has proven instrumental in the study of turbulent boundary layers. Further, not limited to canonical flows, DNSs have been extended to more complex geometries such as airfoils (Vinuesa *et al.* 2017). These simulations have not only led to detailed insights into velocity profiles, turbulence statistics and the near-wall dynamics to name a few, but have also served as a validation to experiments and thereby they have contributed to refining turbulence models, establishing scaling laws and exploring turbulent coherent structures.

In practical engineering applications, the consideration of heat and mass transfer, turbulent mixing, combustion and other related phenomena is crucial for understanding and optimizing various systems (Kozuka, Seki & Kawamura 2009). In these scenarios, scalar quantities such as temperature play a significant role and need to be accurately simulated. Additionally, understanding and predicting the dynamics of passive scalars like air and water pollutants play an important role in local and global environmental problems (Kasagi & Iida 1999; Lazpita *et al.* 2022), as well as in the design of transport and energy systems (Straub *et al.* 2019).

Several experimental studies (Kays 1972; Perry & Hoffmann 1976; Simonich & Bradshaw 1978; Subramanian & Antonia 1981; Krishnamoorthy & Antonia 1987) have analysed different aspects of heat transfer of passive scalars in turbulent boundary layers. The investigation by Kays (1972) presented the variation of skin-friction coefficient and Stanton number (which characterizes the ratio of the heat transfer into the fluid to the thermal capacity of the fluid) in the boundary layer over a transpiring wall, with different blowing and suction conditions for a constant free-stream velocity condition. They have also discussed and proposed theoretical models to enable the prediction of heat transfer in a turbulent boundary layer. A zero-pressure-gradient turbulent boundary layer with constant wall-temperature conditions was set up by Perry & Hoffmann (1976), which enabled them to test similarity relations between instantaneous heat and momentum fluxes. Simonich & Bradshaw (1978) investigated the effects of free stream on heat transfer in a turbulent boundary layer and reported an increase in Stanton number with respect to free-stream turbulence. Subramanian & Antonia (1981) studied the effects of Reynolds number in a turbulent boundary layer and reported the Kármán and additive constants in the logarithmic law for velocity and temperature to be independent of Reynolds number. Further, Krishnamoorthy & Antonia (1987) were able to measure the three components of average temperature dissipation very close to the wall in a turbulent boundary layer, in the effort to model turbulence for the computation of temperature fields. Thereby, the heat-transfer behaviour has been a subject of continuous investigation from both engineering and numerical-modelling perspectives.

In numerical investigations, the fluid temperature can be considered as a passive scalar, provided that the buoyancy effects and the temperature dependence of fluid properties are considered as negligible (Chandrasekhar 1961; Monin & Yaglom 1971). Note that the passive scalar as simulated in the DNS is a diffusive contaminant in the fluid flow. Due to its low concentration, it does not have an influence on the fluid but is influenced by the fluid motion. Although the discussion of passive scalars is in the context of a thermal boundary layer, it could very well be considered as a pollutant concentration, in which case the Schmidt number would be the mass transfer analogous to the Prandtl number. Considering the passive scalar to represent temperature, many DNS studies of turbulent scalar transport have been performed to analyse the convective heat transfer between the fluid and solid walls in spatially developing flows. Bell & Ferziger (1993) first performed the DNS for a turbulent thermal boundary layer. Later, Kong, Choi & Lee (2000) performed a DNS at a Prandtl number of $Pr = 0.71$ with different boundary conditions including isothermal (Dirichlet) and isoflux (Neumann) conditions, for Re_θ ranging between 300 and 420 (note that Re_θ is the Reynolds number based on momentum thickness where the momentum thickness quantifies the loss in momentum due to the presence of a boundary layer). The Reynolds-number range was extended in the studies by Hattori, Houra & Nagano (2007), who simulated Re_θ from 1000 to 1200, at $Pr = 0.71$. At the same time, the numerical investigations for Prandtl numbers up to $Pr = 2$ were performed by Tohdoh, Iwamoto & Kawamura (2008) for a relatively lower Reynolds-number range, up to $Re_\theta = 420$. The effect of different boundary conditions at $Pr = 0.2$, 0.71 and 2.0 in the Reynolds-number range of $Re_\theta \in [350, 830]$ was reported by Li *et al.* (2009). The thermal channel-flow simulations have been conducted at higher Prandtl numbers of 49 and low Re by Schwertfirm & Manhart (2007) and at a Pr of 10 and high Reynolds number by Alcántara-Ávila & Hoyas (2021). However, the thermal turbulent boundary layers have been only partially explored at a medium Prandtl number of 2 by Li *et al.* (2009) owing to the significant computational cost associated with higher Pr. In this study, we consider higher Prandtl numbers in a turbulent thermal boundary layer, reporting analyses that are currently not available in the literature, according to the authors' knowledge. Thereby, the passive scalars at $Pr = 1, 2, 4$ and 6 are simulated for Re_θ up to 1080 in a zero-pressure-gradient turbulent boundary layer using an isothermal wall boundary condition.

The details of the simulation set-up are provided in § 2. The statistics obtained from the simulation at different Prandtl numbers are compared with the data available in the literature for the fully developed thermal turbulent boundary layer in § 3. Since the thermal channel flow and thermal boundary layer exhibit similar behaviours in the near-wall region, the statistical quantities of the channel flow reported in the literature are also compared with the thermal boundary layer quantities at similar Reynolds number. In § 4 we analyse the distribution of energy in different scales for the wall-heat-flux field and wall-parallel fields at $y^+ = 15, 30$ and 50 (where the superscript '+' denotes scaling in terms of friction velocity u_τ, see § 2.4). The premultiplied two-dimensional power-spectral density provides additional insight into the scalar transport at different Prandtl numbers. Finally, a short summary of the observations discussed in this work is reported in § 5.

2. Methodology

2.1. *Governing equations*

A DNS of the zero-pressure-gradient (ZPG) turbulent boundary layer (TBL) is performed using the pseudo-spectral code SIMSON (Chevalier *et al.* 2007). The code solves the governing equations in non-dimensional form (here, written in index notation), in particular the flow and scalar variables are non-dimensionalized as

$$\tilde{x}_j = \frac{x_j}{\delta_0^*}, \quad \tilde{U}_j = \frac{U_j}{U_\infty}, \quad \tilde{t} = \frac{tU_\infty}{\delta_0^*}, \quad \tilde{P} = \frac{P}{\rho U_\infty^2}, \quad \tilde{\Theta}_i = \frac{\Theta_i - \Theta_{i,w}}{\Theta_{i,\infty} - \Theta_{i,w}}, \tag{2.1a–e}$$

where $(x_1, x_2, x_3) = (x, y, z)$ are the Cartesian coordinates in the streamwise, wall-normal and spanwise directions, respectively, and t denotes the time. The length scale used for the non-dimensionalization is the displacement thickness at $x = 0$ and $t = 0$, denoted by δ_0^*. The corresponding instantaneous velocity components are denoted by $(U_1, U_2, U_3) = (U, V, W)$ with the mean quantities identified by $(\langle U\rangle, \langle V\rangle, \langle W\rangle)$ and the fluctuations by (u, v, w). Here U_∞ is the undisturbed laminar free-stream velocity at $x = 0$ and time $t = 0$. The total pressure is denoted by P and the density and kinematic viscosity of the fluid are represented by ρ and ν, respectively. In this study, four different passive scalars $(\Theta_1, \Theta_2, \Theta_3, \Theta_4)$ are simulated at different Prandtl numbers $(Pr = 1, 2, 4, 6)$, respectively. Here, $\Theta_{i,\infty}, \Theta_{i,w}$ correspond to the ith scalar concentration in the free stream and at the wall, respectively, with the mean quantities indicated by $\langle\Theta_i\rangle$ and the corresponding fluctuations by θ_i, $i \in [1, 2, 3, 4]$. The superscript $\tilde{\cdot}$ introduced in (2.1a–e) identifies a non-dimensional variable and it shall be dropped in the non-dimensional quantities for the rest of the sections for simplicity.

The non-dimensional form of the incompressible Navier–Stokes equation and the transport equation for passive scalars are given by

$$\frac{\partial U_j}{\partial x_j} = 0, \tag{2.2}$$

$$\frac{\partial U_j}{\partial t} + U_k \frac{\partial U_j}{\partial x_k} = -\frac{\partial P}{\partial x_j} + \frac{1}{Re_{\delta_0^*}} \frac{\partial^2 U_j}{\partial x_k \partial x_k} + F_j, \tag{2.3}$$

$$\frac{\partial \Theta_i}{\partial t} + U_k \frac{\partial \Theta_i}{\partial x_k} = \frac{1}{Re_{\delta_0^*} Pr} \frac{\partial^2 \Theta_i}{\partial x_k \partial x_k} + F_{\Theta_i}, \tag{2.4}$$

where $Re_{\delta_0^*}$ identifies the Reynolds number based on the free-stream velocity (U_∞) and the displacement thickness at the inlet (δ_0^*). The product of the Reynolds number based on free-stream velocity and the Prandtl number results in another non-dimensional number, called the Péclet number $(Pe = Re_{\delta_0^*} Pr)$, which measures the ratio between the scalar convective transport and the scalar molecular diffusion. Here, F_j and F_{Θ_i} correspond to the volume force terms for the velocity and passive scalars, respectively. The velocity–vorticity formulation of the incompressible Navier–Stokes equation is implemented in the solver as the divergence-free condition is implicitly satisfied by the formulation.

2.2. *Boundary conditions*

Having defined the governing equations, the problem definition is completed by providing appropriate boundary conditions. At the wall, the velocity of the fluid is the same as that of the solid surface and is given by the following no-slip and no-penetration boundary conditions:

$$U|_{y=0} = 0, \quad V|_{y=0} = 0, \quad W|_{y=0} = 0. \tag{2.5a–c}$$

From the continuity equation, we also obtain

$$\left.\frac{\partial V}{\partial y}\right|_{y=0} = 0. \tag{2.6}$$

The flow is assumed to extend to an infinite distance perpendicular to the plate, but discretizing an infinite domain is not feasible. Hence, a finite domain has to be considered, for which artificial boundary conditions have to be applied. A simple Dirichlet condition can be considered; however, the desired flow solution generally contains a disturbance that would be forced to zero. This would introduce an error due to the increased damping of the disturbances in the boundary layer (Lundbladh *et al.* 1999). An improvement to the aforementioned boundary condition can be made by using the Neumann boundary condition given by

$$\left.\frac{\partial U_j}{\partial y}\right|_{y=y_L} = \left.\frac{\partial \mathcal{U}_j}{\partial y}\right|_{y=y_L}, \tag{2.7}$$

where y_L is the height of the solution domain in the wall-normal direction in physical space and $\mathcal{U}_i$ is the laminar base flow that is chosen as the Blasius flow for the present study. For the passive scalars a constant (isothermal) wall boundary condition is applied, as given by

$$\Theta_i|_{y=0} = \Theta_{i,w} = 0, \tag{2.8}$$

which corresponds to a vanishing thermal-activity ratio K. The thermal-activity ratio defines the ratio between the fluid density, thermal conductivity and specific heat capacity and the same properties of the boundary surface as defined below

$$K = \sqrt{\frac{\rho k C_p}{\rho_w k_w C_{p,w}}}. \tag{2.9}$$

Here, ρ_w, k_w and $C_{p,w}$ correspond to the density, thermal conductivity and specific heat capacity of the wall. The isothermal wall boundary condition corresponds to the fluid that exchanges heat with the boundary surface, without modifying the wall temperature. The boundary condition in the free stream is given by

$$\Theta_i|_{y=y_L} = \Theta_{i,\infty} = 1. \tag{2.10}$$

2.3. *Numerical scheme*

The DNS is performed with a pseudo-spectral method, where Fourier expansions are used in the streamwise and spanwise directions and Chebyshev polynomials $T_k(\xi)$ (on $-1 \leq \xi \leq 1$) are used in the wall-normal direction employing the Chebyshev-tau method for faster convergence rates. The time advancement is performed using the second-order Crank–Nicholson scheme for linear terms and the third-order Runge–Kutta method for nonlinear terms, with a constant time step Δt. The maximum Courant number is set to 0.6. The nonlinear terms are calculated in physical space and the aliasing errors in the evaluation of these terms are removed by the 3/2 rule.

Since the TBL is developing in x, the periodic boundary condition cannot be directly used in this particular direction, which requires a specific numerical treatment. In this regard, one approach is to impose an appropriate instantaneous velocity and scalar profile at the inlet for every time step. Assuming self-similarity of the flow in the streamwise direction, Lund, Wu & Squires (1998) proposed a rescaling–recycling method to generate the required inlet profiles based on the solution downstream. An alternative approach is the addition of the fringe region downstream of the physical domain to retain the periodicity in the streamwise direction as described by Bertolotti, Herbert & Spalart (1992); Nordström, Nordin & Henningson (1999). In this method, the disturbances are damped, and the flow is forced from the outflow of the physical domain to the same profile as the inflow. The fringe technique is used in the present study, as the inflow conditions from a laminar profile followed by tripping produce natural instantaneous fluctuations for the velocity and the scalar fields (Araya & Castillo 2012). The fringe region is implemented by adding a volume force (F_j; F_{Θ_i}) to the momentum and scalar transport equations ((2.3) and (2.4)), respectively. The forcing term is given by

$$F_j = \lambda(x)\left(\mathcal{U}_j - U_j\right), \tag{2.11}$$

$$F_{\Theta_i} = \lambda(x)\left(\breve{\Theta}_i - \Theta_i\right), \tag{2.12}$$

where $\lambda(x)$ is the strength of the forcing, which is non-zero only in the fringe region. The flow field at the inlet is the laminar Blasius profile $\mathcal{U}_j$ and for the scalar Θ_i it is the linear variation with y ranging from 0 to 1, denoted by $\breve{\Theta}_i$.

2.4. *Computational domain and numerical set-up*

The laminar base flow is tripped by a random volume force strip (at $x/\delta_0^* = 10$) to trigger the transition of the flow to a turbulent state. For this simulation, a three-dimensional cuboid is considered with length, height and width equal to x_L, y_L, z_L, respectively. The lower surface of the cuboid is considered as a flat plate with no-slip boundary conditions. The boundary layer grows in the considered computational domain with initial thickness denoted by δ_0^*. In the streamwise direction, the computational domain terminates with the fringe region. The vertical extent of the computational domain includes the whole boundary layer and the domain height is chosen based on the free-stream boundary condition. In particular, the problem set-up in this work is similar to that studied by Li *et al.* (2009).

The computational domain is discretized by N_x, N_y and N_z grid points in the streamwise, wall-normal and spanwise directions, respectively. The grid spacing is uniform in the streamwise and spanwise directions. For the wall-normal direction, the collocation points follow the Gauss–Lobatto distribution given by

$$y_c = \cos\left(\pi \frac{c}{N_y}\right) \quad c = 0, 1, 2, \ldots, N_y. \tag{2.13}$$

The computational box has dimensions $1000\delta_0^* \times 40\delta_0^* \times 50\delta_0^*$ in the streamwise, wall-normal and spanwise directions, respectively. The number of grid points in each direction is 3200 × 385 × 320, correspondingly. Note that the smallest scale in the scalar fluctuations is inversely proportional to $Pr^{1/2}$ (Tennekes & Lumley 1972) and, hence, the Batchelor length scale η_{Θ_i} (which is analogous to the smallest scale in turbulent flow, the Kolmogorov scale η) is estimated as $\eta Pr^{-1/2}$ (Kozuka *et al.* 2009). Similarly, the ratio of the largest to the smallest scales is proportional to $Re^{1.5}Pr^{0.5}$ at high Pr (Batchelor 1959; Tennekes & Lumley 1972). In this study, an adequate grid resolution is adopted to resolve all the physically relevant scales. The Reynolds number based on free-stream velocity and displacement thickness at the inlet is $Re_{\delta_0^*} = 450$ and the friction Reynolds number based on local friction velocity (u_τ) and boundary-layer thickness (δ_{99}) is $Re_\tau = 46$. At the outlet, the Reynolds number based on displacement thickness is $Re_{\delta_0^*} = 1,580$ and $Re_\tau = 396$.

Considering the friction velocity u_τ at the middle of the computational domain ($x/\delta_0^* = 500$, corresponding to $Re_\theta = 794$), the grid resolution in viscous units is $\Delta x^+ = 6.6$ and $\Delta z^+ = 3.3$ in the wall-parallel directions. In the wall-normal direction, we have an irregular distribution of collocation points, hence Δy^+ varies between 0.01 and 3.5. The results discussed at a particular streamwise position are inner scaled with respect to the local friction velocity, whereas, when the data along the streamwise direction are considered, the reference quantity at $x/\delta_0^* = 500$ is considered for inner scaling. This indicates that if a particular wall-parallel plane (x–z plane) is sampled at a wall-normal distance (for e.g. $y^+ = y_s$), considering the friction velocity at $x/\delta_0^* = 500$, the actual inner-scaled location varies along the streamwise direction, which is within $\pm 0.1 y_s$ for the range of Reynolds numbers simulated in this work.

In this study, five different realizations of ZPG TBL are performed by introducing different trip forcings through modification of the random seed parameter, to obtain an ensemble average of the statistical quantities. All the different realizations are run for approximately 2400 time units (δ_0^*/U_∞) after one flow through of initial transience, which corresponds to 1000 time units (δ_0^*/U_∞). The converged statistics are obtained with the data corresponding to 12,000 time units (δ_0^*/U_∞), equivalent to 600 eddy-turnover times.

3. Comparison with data in the literature

3.1. *Integral quantities and non-dimensional numbers*

The shape factor H_{12}, which measures the ratio between the displacement thickness δ^* and the momentum thickness θ, is plotted in figure 1. The shape factor is lower in the turbulent region with increasing Re_θ and agrees well with the experimental and numerical data for $Re_\theta > 600$ where the TBL is fully developed.

Figure 2 depicts the streamwise variation of the skin-friction coefficient C_f for the present simulation and indicates that the obtained result is in good agreement with the turbulent skin-friction solution provided by Schoenherr (1932), which is given by

$$C_f = 0.31 \left[\ln^2 (2Re_\theta) + 2 \ln (2Re_\theta) \right]^{-1}. \tag{3.1}$$

The computed skin-friction coefficient is also in good agreement with the correlation proposed by Smits, Matheson & Joubert (1983), which is given as

$$C_f = 0.024 Re_\theta^{-1/4}. \tag{3.2}$$

The trip location is at $x/\delta_0^* = 10$, with a strong peak in the skin-friction coefficient followed by the transition to turbulence before $x/\delta_0^* = 200$. The experimental data

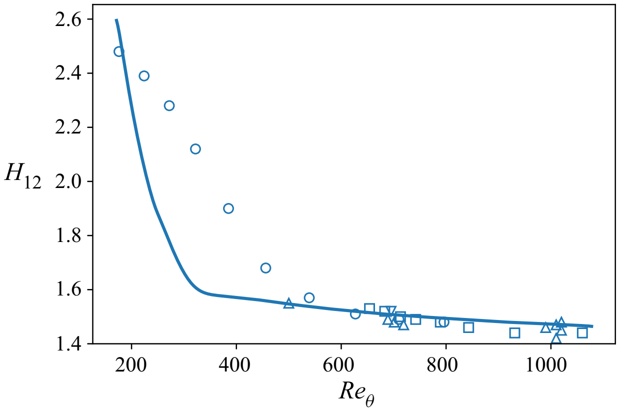

Figure 1. Streamwise evolution of the shape factor H_{12}. (——, blue) Present DNS, (□, blue) Simens *et al.* (2009), experimental data by (○, blue) Roach & Brierly (1992), (△, blue) Erm & Joubert (1991), (▽, blue) Purtell, Klebanoff & Buckley (1981).

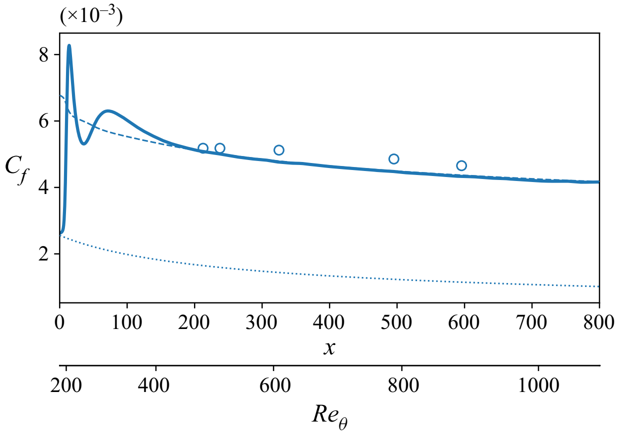

Figure 2. Variation of skin-friction coefficient along the streamwise direction. (——, blue) Present DNS, (······, blue) theoretical laminar skin-friction solution, (- - -, blue) turbulent solution given by Schoenherr (1932), (○, blue) experimental data by Erm & Joubert (1991) with wire tripping.

provided by Erm & Joubert (1991) with wire tripping also closely correspond to the calculated turbulent skin-friction coefficient. It should be noted that Erm & Joubert (1991) also repeated the experiments with different tripping devices and found the influence of tripping to persist until $Re_\theta \approx 1500$. Due to this, Jiménez *et al.* (2010) found the experimental data to be scattered for $Re_\theta < 1070$ and also showed the scatter to decrease with $Re_\theta > 1600$.

The Stanton number measures the convective heat transfer into the fluid with respect to the thermal capacity of the fluid. The spatial evolution of the Stanton numbers for different passive scalars scaled with the square root of Pr (as plotted in figure 3) is very similar to the skin-friction profiles plotted in figure 2. There is a difference observed in the laminar Stanton number at $x = 0$ with the present scaling. However, the individual Stanton-number profiles correspond well to the laminar solution (not shown in the figure) given by Kays &

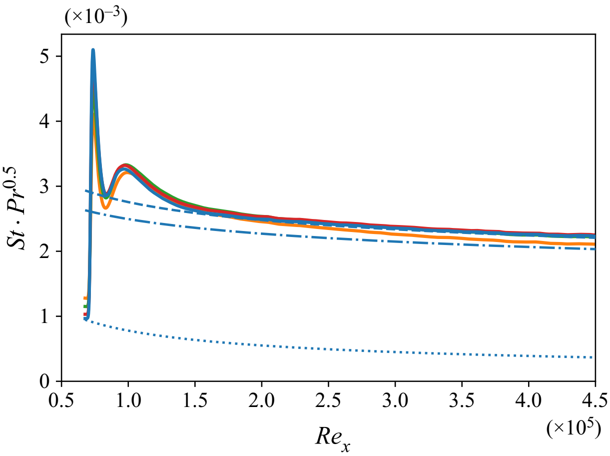

Figure 3. Variation of Stanton number along the streamwise direction for different passive scalars. (——, orange) Θ_1 , (——, green) Θ_2, (——, red) Θ_3, (——, blue) Θ_4, (······, blue) Kays & Crawford (1993) correlation corresponding to Θ_4 and (- - -, blue) Reynolds–Colburn analogy as given by Lienhard & John (2005) plotted for Θ_4, (—·, blue) interpolation developed by Hollingsworth (1989) plotted for Θ_4.

Crawford (1993), which is

$$St = \frac{0.332}{\sqrt{Re_x} Pr^{2/3}}, \tag{3.3}$$

and to the turbulent solution obtained from the Reynolds–Colburn analogy as given by Lienhard & John (2005). For Θ_1, due to the Reynolds analogy, the Stanton profile matches with the skin-friction profile scaled by a factor of two. For the passive scalars at higher Prandtl numbers, a generalization of the Reynolds–Colburn analogy can be obtained, as reported in the study by Lienhard (2020)

$$St = \frac{Nu}{Re_x Pr} = \frac{C_f/2}{a_1 + a_2\,(Pr^{a_3} - 1)\sqrt{C_f/2}}, \tag{3.4}$$

with the values of $a_1 = 1$, $a_2 = 12.8$ and $a_3 = 0.68$ provided in Lienhard & John (2005) and C_f being expressed as

$$C_f = \frac{0.455}{\ln^2 (0.06 Re_x)}. \tag{3.5}$$

The Stanton-number plot for the passive scalar at $Pr = 6$ agrees well with the turbulent solution obtained from the Reynolds–Colburn analogy, as shown in figure 3. On the other hand, reference curves for Kays & Crawford and the Reynolds–Colburn analogy are only reported for Θ_4 for clarity.

Using the data for water with $Pr = 5.9$, Hollingsworth (1989) developed an interpolation for Prandtl numbers from 0.7 to 5.9 assuming the critical thickness of the sub-layer to be a simple function of Prandtl number. The empirical expression is given by

$$St = 0.02426 Pr^{-0.895} Re_x^{-0.1879 Pr^{-0.18}}, \tag{3.6}$$

which is plotted for the scalar at $Pr = 6$ in figure 3. We find that the relationship proposed by Hollingsworth (1989) underpredicts the Stanton number at $Pr = 6$. However, the

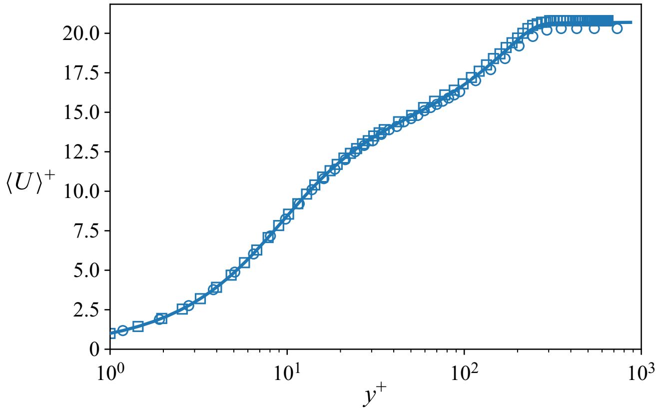

Figure 4. Inner-scaled mean streamwise velocity profile at $Re_\theta = 670$. (——, blue) Present DNS, (○, blue) Spalart (1988), (□, blue) Komminaho & Skote (2002) at $Re_\theta = 666$.

interpolation relation provides a good match with the calculated Stanton number for Θ_1, better than the Reynolds–Colburn analogy, which is not indicated in the plot for clarity.

Using the data obtained in the present simulation, a correlation between the Nusselt, Prandtl and Reynolds numbers can be obtained as

$$Nu_x = 0.02 Re_x^{0.828} Pr^{0.514}, \tag{3.7}$$

which yields $R^2 = 0.9985$. This is similar to the correlation proposed by Kays & Crawford (1993) but for fully developed profiles in circular tubes and computed for gases

$$Nu = 0.021 Re^{0.8} Pr^{0.5}. \tag{3.8}$$

3.2. *Mean velocity and scalar profiles*

The mean velocity profile obtained at the streamwise location corresponding to $Re_\theta = 670$ is shown in figure 4. The streamwise velocity profile is compared with the DNS data from Spalart (1988) at $Re_\theta = 670$ and Komminaho & Skote (2002) at $Re_\theta = 666$. The comparison of the present data with the existing DNS results shows a good agreement in the inner region. There is a slight deviation of the mean velocity profile reported by Spalart (1988) in the wake region with respect to the present data but it agrees well with the data provided by Komminaho & Skote (2002).

The mean profiles of the various passive scalars Θ_i are normalized with the respective Prandtl numbers and represented in inner scaling by dividing with the friction scalar $\Theta_{i,\tau}$ defined as

$$\Theta_{i,\tau} = \frac{q_{i,w}}{\rho C_p u_\tau}, \tag{3.9}$$

where C_p is the heat capacity of the fluid and $q_{i,w}$ is the rate of heat transfer from the wall to the fluid and is defined by

$$q_{i,w} = -k \left.\frac{\mathrm{d}\langle\Theta_i\rangle}{\mathrm{d}y}\right|_{y=0}, \tag{3.10}$$

where k is the thermal conductivity of the fluid. The normalized inner-scaled mean scalar profiles are plotted at $Re_\theta = 1070$, corresponding to $Re_\tau = 395$, as shown in figure 5.

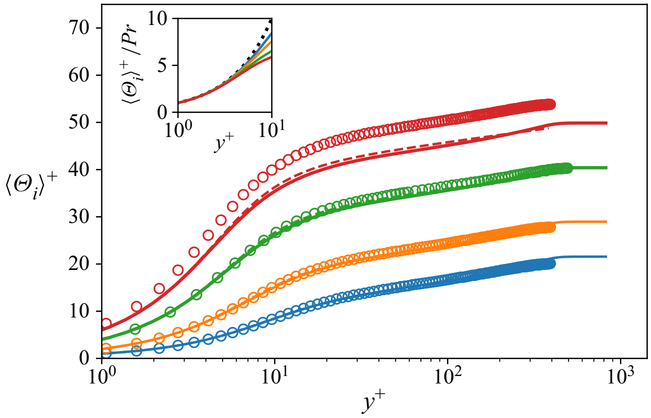

Figure 5. Normalized mean profiles of the passive scalars at $Re_\theta = 1070$ corresponding to $Re_\tau = 395$. (——, blue) $Pr = 1$, (——, orange) $Pr = 2$, (——, green) $Pr = 4$, (——, red) $Pr = 6$, channel DNS data by Kozuka *et al.* (2009) at $Re_\tau = 395$ and (○, blue) $Pr = 1$, (○, orange) $Pr = 2$, (○, red) $Pr = 7$, (○, green) channel DNS data by Alcántara-Ávila, Hoyas & Pérez-Quiles (2018) at $Re_\tau = 500$ and $Pr = 4$, with (- - -, grey) corresponding fit by Pirozzoli (2023) and (inset) (· · · · · ·, black) conductive sub-layer relation, $\Theta_i^+ = Pry^+$.

The mean scalar profiles follow the conductive sub-layer relation ($\Theta_i^+ = Pry^+$) and is clearly identified in the plots for $y^+ < 5$. The profiles of the passive scalars at $Pr = 1, 2$ are compared against the channel DNS data provided by Kozuka *et al.* (2009) at the same Prandtl numbers. The comparison shows a good agreement in the near-wall and overlap regions. It should be noted that the boundary condition used by Kozuka *et al.* (2009) is the uniform-heat-flux condition as opposed to the uniform scalar boundary condition applied in this study. Note that the study by Kawamura, Abe & Shingai (2000) showed that the Kármán constant k_Θ as appearing in (3.11)

$$\frac{\langle \Theta_i \rangle - \langle \Theta_{i,w} \rangle}{\Theta_{i,\tau}} = \frac{1}{k_\Theta} \log y^+ + A_{\Theta_i}(Pr), \tag{3.11}$$

varies between the Dirichlet and Neumann boundary conditions based on low-Reynolds-number simulations. Here, A_{Θ_i} denotes the additive constant for scalar Θ_i. However, based on higher-Reynolds-number simulations, Pirozzoli, Bernardini & Orlandi (2016) reported that the difference in boundary condition affects the mean passive scalar profiles only in small magnitudes in the logarithmic region, although the effect is evident in the scalar fluctuation profiles reported later.

The scalar profile at $Pr = 4$ is compared against the channel DNS data reported by Alcántara-Ávila *et al.* (2018). The channel DNS data reported by Kozuka *et al.* (2009) at $Pr = 7$ are used for comparison of the passive scalar at $Pr = 6$, since there are no simulations reported in the literature at exactly the same Prandtl number. This gives us the opportunity to highlight the difference between the profiles at these high Prandtl numbers. Due to the difference in the considered Prandtl numbers, we observe a discrepancy in the mean velocity profile for $y^+ > 40$ in the overlap region. Since the channel data are used for the comparison, there is a difference observed near the wake region for all the cases. However, a good agreement of the profiles is observed for the inner region. Based on experimental data, semi-empirical fits were provided by Kader (1981) for a boundary layer with constant heat flux. In this study it was assumed that the overlap layer exhibited logarithmic variation as given in (3.11), and an empirical relation was provided to determine the additive constant B_{Θ_i}. The comparison of the mean scalar profiles against the relationships provided by Kader (1981) shows that the value at the wake is slightly overestimated with respect to the DNS data. The deviation for scalar Θ_4 corresponding to $Pr = 6$ is approximately 3 % for $y^+ \in [100, 500]$. One possible reason for this small deviation could also be the constant scalar boundary condition imposed in our simulations as opposed to the constant-heat-flux boundary conditions considered by Kader (1981). The comparison against Kader (1981) is not presented, instead, the mean scalar profiles are evaluated against the recent correlations proposed by Pirozzoli (2023). These correlations were developed by fitting the functional form of eddy thermal diffusivity to DNS data, resulting in predictive formulae for mean scalar profiles. Our comparison demonstrates good agreement across the different Prandtl numbers. For the passive scalar Θ_4, the maximum observed deviation is approximately 2 %.

In the overlap region, the mean scalar profiles are nearly logarithmic and are characterized as

$$\langle \Theta_i \rangle^+_\infty - \langle \Theta_i \rangle^+ = -\frac{1}{k_\Theta} \log\left(y/\delta^*\right) + B_{\Theta_i}(Pr) . \tag{3.12}$$

The mean scalar and velocity profiles are plotted in defect form in figure 6. We observe that the slope of the scalar profiles in defect form is nearly parallel indicating a constant Kármán constant for the scalar fields. The Kármán constant for the velocity is observed to be 0.41, consistent with the values reported in Spalart (1988). The diagnostic function for scalar is defined as

$$\varXi_\Theta = y^+ \frac{\partial \langle \Theta_i \rangle^+}{\partial y^+} = \frac{1}{k_\Theta}, \tag{3.13}$$

is plotted in figure 7. The Kármán constant for a scalar field is obtained as $k_\Theta = 0.4$, which is in between $k_\Theta = 0.33$ (Wikström 1998) and $k_\Theta = 0.47$ (Kader 1981). The obtained k_Θ from the present simulation is the same as observed by Kawamura, Abe & Matsuo (1999) and close to the value of 0.41 as reported by Li *et al.* (2009). In the outer region, we observe a collapse of the profiles.

3.3. *Velocity and scalar fluctuations*

As shown in figure 8, the present velocity-fluctuation root-mean-squared (r.m.s.) data show a trend similar to that of the results by Jiménez *et al.* (2010). The r.m.s. profiles of the three velocity components are in good agreement in the inner region, while a minor difference can be observed in the outer region. Nonetheless, the peaks of the velocity fluctuations match in both position and magnitude. There is a slight offset in the plots of p_{rms}, which can be attributed to the small difference in the considered Re_θ for comparison. The r.m.s. of the velocity components are also compared with the channel DNS data provided by Abe *et al.* (2004). The streamwise r.m.s. agrees well with the present DNS results and the near-wall peak value coincides with the present observations. As expected, there is a difference observed in the outer region of flow, since channel and boundary-layer flows are fundamentally different farther from the wall. Additionally, the r.m.s. of the pressure fluctuations observed in the boundary layer is different compared with the channel flow. From the present DNS data, the peak of the streamwise velocity fluctuation is found at $y^+ = 14$, corresponding in outer units to $y/\delta_{99} = 0.035$.

The r.m.s. of the scalars at different Prandtl numbers are plotted in figure 9. The scalar r.m.s. profile at $Pr = 1$ is similar to the streamwise velocity r.m.s. and has a higher (roughly 5 %) near-wall peak comparatively, as expected. The comparison of scalar-fluctuation

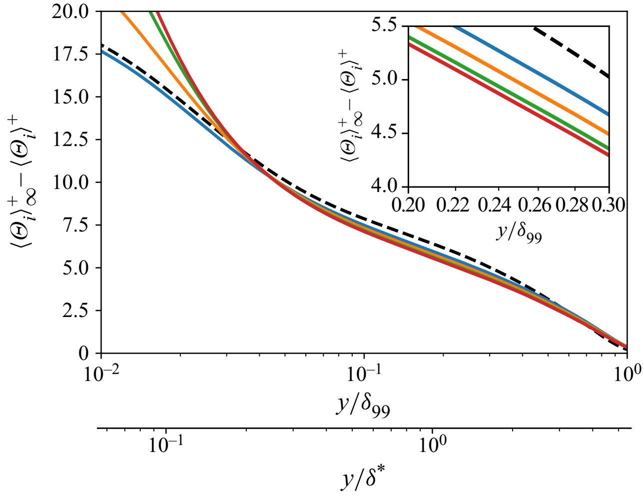

Figure 6. Mean profiles in defect form at $Re_\theta = 1070$ corresponding to $Re_\tau = 395$. (——, blue) $Pr = 1$, (——, orange) $Pr = 2$, (——, green) $Pr = 4$, (——, red) $Pr = 6$ and (- - -, black) velocity defect $\langle U_\infty \rangle^+ - \langle U \rangle^+$.

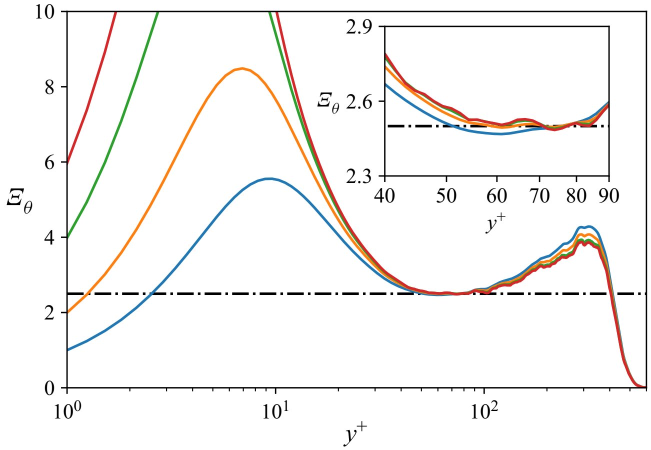

Figure 7. Variation of the diagnostic function for scalar Ξ_Θ along the wall-normal direction at $Re_\theta = 1070$ corresponding to $Re_\tau = 395$. (——, blue) $Pr = 1$, (——, orange) $Pr = 2$, (——, green) $Pr = 4$, (——, red) $Pr = 6$ and (—·, black) $\Xi_\Theta = 0.25;\ k_\Theta = 0.4$.

profiles at $Pr = 1, 2$ with the channel DNS data from Kozuka *et al.* (2009) shows a good agreement in the inner and logarithmic region in addition to a good match of the peak value and wall-normal location. Despite the small difference in Re_τ, the profiles at $Pr = 4$ obtained by Alcántara-Ávila *et al.* (2018) show a reasonably good agreement with the present results. With increasing Prandtl number, the peak value of the scalar-fluctuation r.m.s. increases and is located closer to the wall. The scalar fluctuations decay to zero at the wall due to the isothermal boundary condition and they also decay to zero outside the boundary layer due to the absence of disturbances in the free stream.

The obtained scalar-fluctuation r.m.s. profiles are scaled with the respective Prandtl numbers and plotted in figure 10. We observe that the lines of $\theta^+_{i\,rms}$ for different scalars at different Reynolds numbers are parallel and not coinciding. Similar observations were

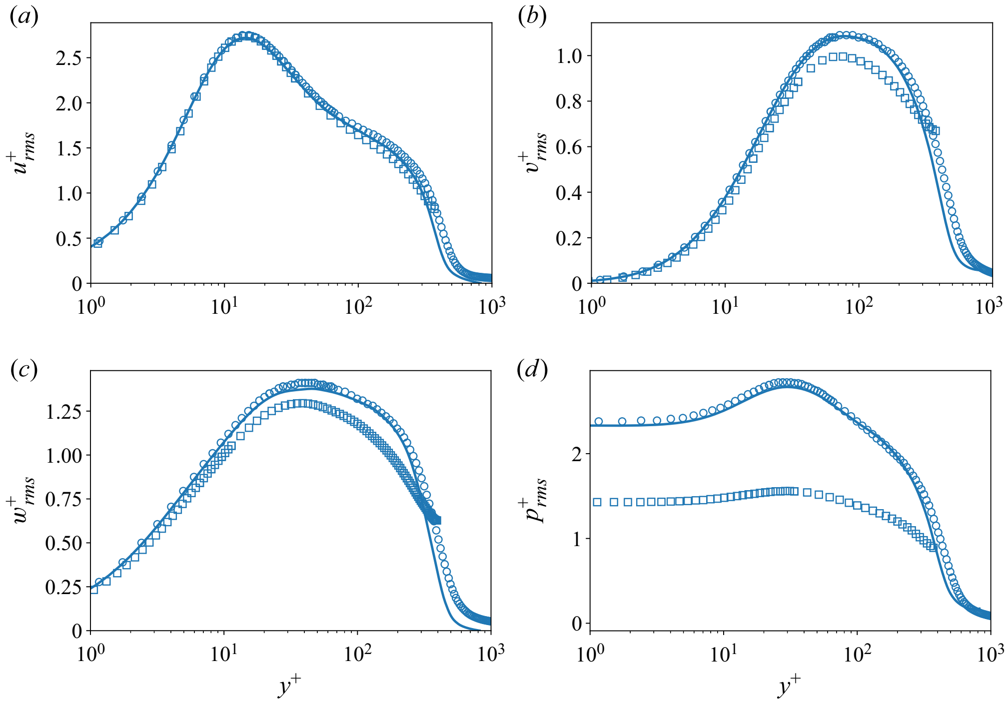

Figure 8. The r.m.s. velocity fluctuations and r.m.s. pressure fluctuation at $Re_\theta = 1070$. (——, blue) Present DNS, (○, blue) Jiménez *et al.* (2010) at $Re_\theta = 1100$, (□, blue) channel DNS data of Abe, Kawamura & Matsuo (2004) at $Re_\tau = 395$.

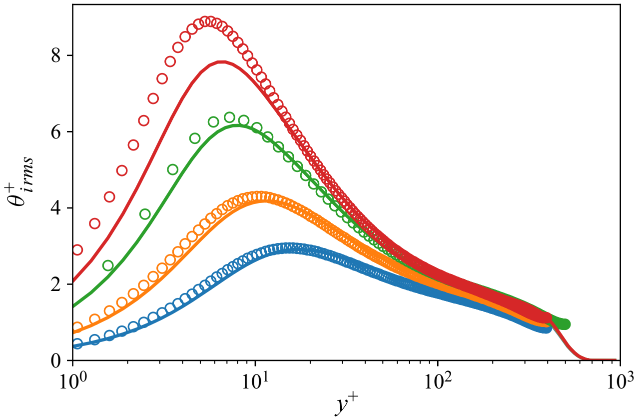

Figure 9. Scalar fluctuation r.m.s. at $Re_\theta = 1070$. Present DNS data for (——, blue) $Pr = 1$, (——, orange) $Pr = 2$, (——, green) $Pr = 4$, (——, red) $Pr = 6$, channel DNS data by Kozuka *et al.* (2009) at $Re_\tau = 395$ and (○, blue) $Pr = 1$, (○, orange) $Pr = 2$, (○, red) $Pr = 7$, (○, green) channel DNS data by Alcántara-Ávila *et al.* (2018) at $Re_\tau = 500$ and $Pr = 4$.

also made by Alcántara-Ávila, Hoyas & Pérez-Quiles (2021) for a particular scalar at $Pr = 0.71$ and they attributed the differences in the viscous-diffusion term at the wall to the increase in the slope of $\theta^+_{i\,rms}$. The slope of $\theta^+_{i\,rms}$ changes with Reynolds number because the peak of $\theta^+_{i\,rms}$ varies as shown in figure 11 and the location of such a peak moves

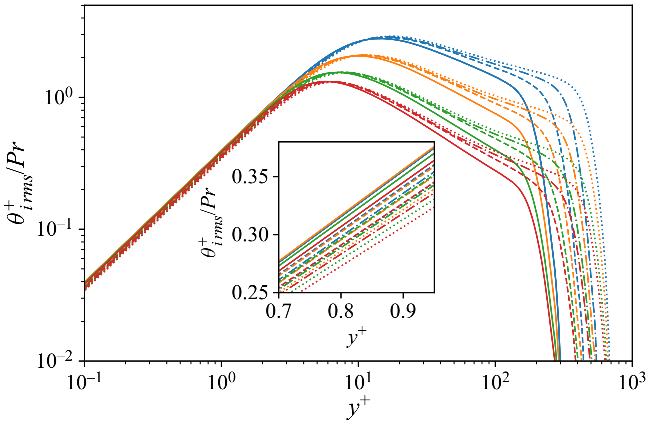

Figure 10. Scalar fluctuations scaled by Prandtl number at (——, blue) $Pr = 1$, (——, orange) $Pr = 2$, (——, green) $Pr = 4$, (——, red) $Pr = 6$ and (——, black) $Re_\theta = 420$, (- - -, black) $Re_\theta = 628$, (—·, black) $Re_\theta = 830$, (······, black) $Re_\theta = 1070$ at the corresponding Prandtl numbers.

farther from the wall as the Reynolds number increases. On the other hand, the location of $\theta^+_{i\,rms,max}$ moves closer to the wall with respect to the Prandtl number, as discussed earlier. A correlation for $\theta^+_{i\,rms,\,max}$ was obtained as in Alcántara-Ávila *et al.* (2021) for each passive scalar considered in the present study, as shown in figure 11. It should be noted that if the maximum value is obtained directly at the collocation point, some variations are observed along Re_τ due to the grid resolution. In order to minimize the high-frequency variation along Re_τ, as plotted in figures 11 and 12, a simple convolution operation is performed which does not alter the obtained empirical fits. Clearly, for higher Prandtl numbers of 4, 6, the peak of the scalar-fluctuation r.m.s. tends to decrease with increasing Re_τ. When the present DNS data with $Re_\theta \in [470, 1070]$ and $Pr = 1, 2, 4, 6$ are used to find an overall variation of the peak in the scalar-fluctuation r.m.s. we find

$$\theta^+_{i\,rms,max}=2.969Re_\tau^{-0.00858}Pr^{0.571}, \tag{3.14}$$

with $R^2 = 0.99$, where R^2 corresponds to the coefficient of determination. It is defined as $R^2 = 1 - (\Sigma(x_t - x_p)^2)/(x^2_{t\,rms})$, with x_p corresponding to the fitted value of x_t. The observed correlation shows a weak dependence on Re compared with Pr. Further, from (3.14), a decaying trend of $\theta^+_{i\,rms,max}$ with Re is obtained, although such a trend has not been observed in the literature except for Θ_3, Θ_4 in the present study. The studies by Pirozzoli *et al.* (2016) and Alcántara-Ávila *et al.* (2021) have reported the increasing trend of $\theta^+_{i\,rms,max}$ with respect to Re but for a lower Pr than in the present work. Pirozzoli *et al.* (2016) have suggested that the attached-eddy arguments support the increase of inner peak of streamwise velocity r.m.s. with respect to Re_τ due to the effect of overlying attached eddies and they assumed that the same argument applies to the passive scalars. On the other hand, we find that the inner peak of the passive scalar r.m.s. at high Pr does not follow the previous argumentation. It should also be noted that the range of Re_τ in our present simulation is narrow compared with those of the works by Pirozzoli *et al.* (2016) and Alcántara-Ávila *et al.* (2021) and a more detailed investigation of this topic is necessary to make any conclusive statements.

The above procedure was also performed for the streamwise heat flux, as shown in figure 12. A similar behaviour was observed with the overall variation in streamwise heat

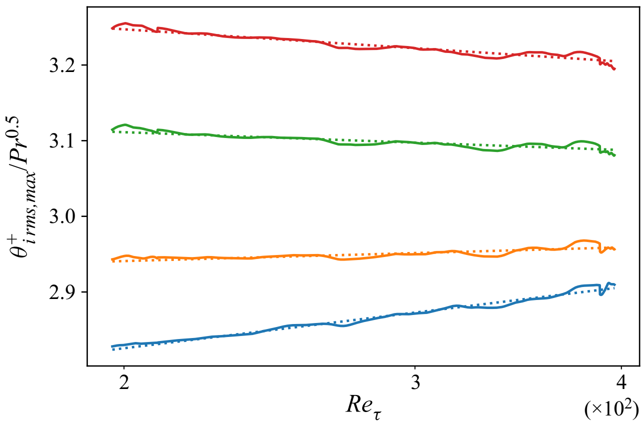

Figure 11. Variation of the peak of scalar fluctuation r.m.s. with respect to Re_τ, for (——, blue) $Pr = 1$, (——, orange) $Pr = 2$, (——, green) $Pr = 4$, (——, red) $Pr = 6$ including the corresponding empirical fits (······, blue) $0.116 \log{(Re_\tau)} + 2.210$ with $R^2 = 0.976$, (······, orange) $0.037 \log{(Re_\tau)} + 3.963$ with $R^2 = 0.620$, (······, green) $-0.068 \log{(Re_\tau)} + 6.583$ with $R^2 = 0.726$, (······, red) $-0.151 \log{(Re_\tau)} + 8.753$ with $R^2 = 0.894$.

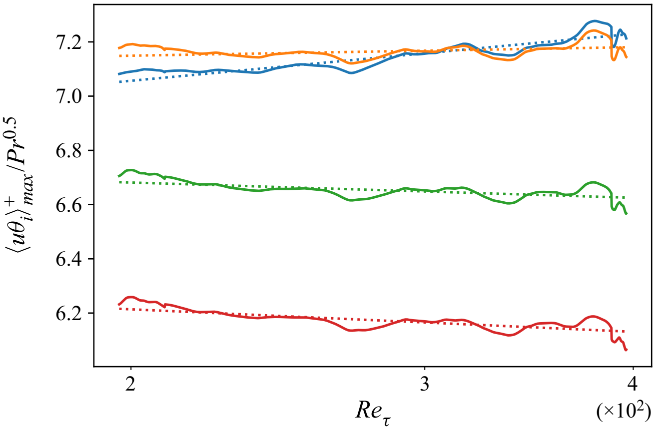

Figure 12. Variation of the peak of streamwise heat flux with respect to Re_τ, for (——, blue) $Pr = 1$, (——, orange) $Pr = 2$, (——, green) $Pr = 4$, (——, red) $Pr = 6$ including the corresponding empirical fits (······, blue) $0.250 \log{(Re_\tau)} + 5.732$ with $R^2 = 0.808$, (······, orange) $0.064 \log{(Re_\tau)} + 9.769$ with $R^2 = 0.119$, (······, green) $-0.1626 \log{(Re_\tau)} + 14.223$ with $R^2 = 0.328$, (······, red) $-0.293 \log{(Re_\tau)} + 16.773$ with $R^2 = 0.513$.

flux given by

$$\langle u\theta_i\rangle^+_{max} = 7.74 Re_\tau^{-0.006} Pr^{0.401}, \tag{3.15}$$

with $R^2 = 0.9913$.

3.4. *Turbulent Prandtl number*

An important parameter for scalar transport is the turbulent Prandtl number Pr_t, which is defined as the ratio between turbulent eddy viscosity and turbulent eddy diffusivity

$$Pr_t = \frac{\nu_t}{\alpha_t}. \tag{3.16}$$

The eddy viscosity and the eddy diffusivity arise from the Boussinesq hypothesis (Boussinesq 1877) for modelling turbulent stresses and the heat-flux vector, respectively. For parallel flows (the ones in which the velocity profile does not vary in the streamwise direction), the turbulent eddy viscosity and the turbulent eddy diffusivity are used to describe the turbulent momentum transfer and heat transfer with respect to the mean-flow conditions, in particular the mean velocity strain and temperature gradients, respectively. They are defined as

$$\nu_t = -\frac{\langle uv \rangle}{\partial \langle U \rangle / \partial y}, \tag{3.17}$$

and

$$\alpha_t = -\frac{\langle v\theta_i \rangle}{\partial \langle \Theta_i \rangle / \partial y}. \tag{3.18}$$

It should be noted that the eddy viscosity or diffusivity does not represent a physical property of the fluid, like the molecular viscosity, but rather a property of the flow. The Reynolds analogy introduces the similarity between the turbulent momentum exchange and turbulent heat transfer in a fluid. Reynolds (1874) noted that, for a fully turbulent field, both the momentum and heat are transferred due to the motion of turbulent eddies. This yields a simpler model for the turbulent Prandtl number, where the turbulent eddy viscosity for the momentum exchange and turbulent eddy diffusivity for the scalar transport are equal, such that $Pr_t = 1$.

Substitution of the eddy viscosity and diffusivity into the definition of turbulent Prandtl number results in

$$Pr_t = \frac{\langle uv \rangle}{\langle v\theta_i \rangle} \frac{\partial \langle \Theta_i \rangle / \partial y}{\partial \langle U \rangle / \partial y}. \tag{3.19}$$

From this definition, evaluating the turbulent Prandtl number at any point in the boundary layer would require the turbulent shear stress, turbulent heat transfer, velocity gradient and temperature gradient. Experimental investigations have limited accuracy in the simultaneous measurement of the Reynolds shear stress and wall-normal turbulent heat flux, in particular close to the wall (Araya & Castillo 2012). For this reason, experimental investigations like Blom (1970), Antonia (1980) and Kays & Crawford (1993) exhibit significant scatter in the data.

The variation of turbulent Prandtl number with the wall-normal distance in inner units at a given $Re_\theta = 1070$ is reported in figure 13. We observe that the turbulent Prandtl number varies at the wall and increases with respect to molecular Prandtl number of the scalar. From figure 14, we also see the turbulent Prandtl number decays for $y^+ > 15$ and this decay becomes steeper as Re decreases. The turbulent Prandtl number was assumed to approach a constant value close to the wall independent of the molecular Prandtl number (Li 2007). Studies such as the ones by Kestin & Richardson (1963) and Blom (1970) have analysed experimentally the turbulent Prandtl number in order to assess the validity of this assumption. Such experimental investigations have reported a constant value of turbulent Prandtl number as the wall is approached. However, different experimental campaigns provided data that could not show a conclusive interpretation of the behaviour of turbulent Prandtl number close to the wall. Nonetheless, many authors have proposed different correlations based on the experimental data to predict the heat-transfer coefficient through the prediction of turbulent Prandtl number with respect to molecular Prandtl number.

For the different passive scalars considered in the present study, the turbulent Prandtl number approaches a constant value > 1 close to the wall in the viscous sub-layer. The plots of Pr_t exhibit a significant difference closer to the wall with respect to various

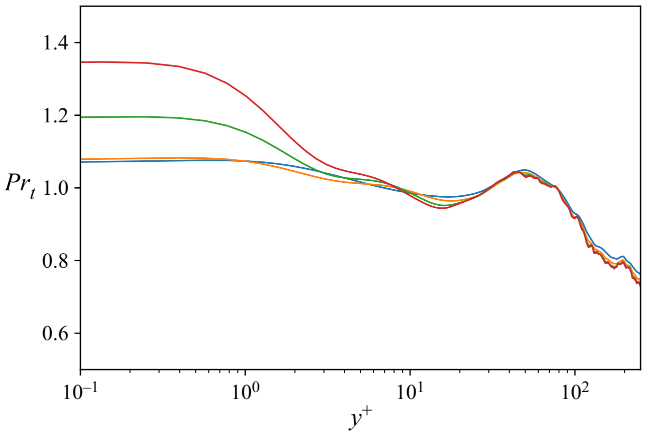

Figure 13. Variation of turbulent Prandtl number with respect to wall-normal distance in inner scale at $Re_\theta = 1070$ for passive scalar at (——, blue) $Pr = 1$, (——, orange) $Pr = 2$, (——, green) $Pr = 4$, (——, red) $Pr = 6$.

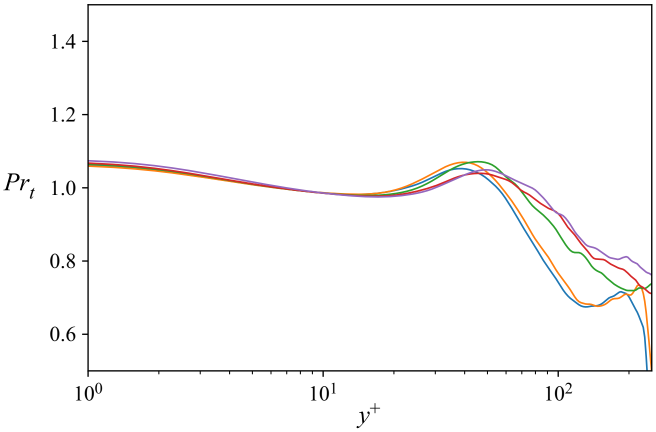

Figure 14. Variation of turbulent Prandtl number with respect to wall-normal distance in inner scale at (——, blue) $Re_\theta = 396$, (——, orange) $Re_\theta = 420$, (——, green) $Re_\theta = 628$, (——, red) $Re_\theta = 830$, (——, purple) $Re_\theta = 1070$ for a passive scalar at $Pr = 1$.

molecular Prandtl numbers. There is a slight decrease in Pr_t up to $y^+ \approx 20$ and then the increase is maintained farther from the wall up to $y^+ \approx 50$, the point after which the trend steadily decreases. It is pointed out in Kays (1994) that the peak between $y^+ \approx 20$ and 100 is not observed in the experimental data, an observation which was attributed to the high Reynolds number of the experiments, where DNS data are not available for comparison.

Following the discussions about a constant Pr_t in the logarithmic region, Kays & Crawford (1993) proposed a correlation for the turbulent Prandtl number that is applicable to air. In this correlation, the value of Pr_t approaches a constant value of 0.85 in the logarithmic region. In the studies by Hollingsworth (1989), a correlation was proposed based on the measurement of the temperature profile of water at $Pr \approx 6$. Again, the value of Pr_t approaches a value of 0.85 as y^+ is increased. This observation of constant Pr_t in the logarithmic region is not clearly observed with the present DNS data. This can be due to the low-Reynolds-number range considered in the present study. Based on the correlation proposed by Hollingsworth (1989), Kays (1994) suggested a constant value of $Pr_t = 1.07$ for $0 < y^+ < 5$. Indeed, if we consider only the passive scalars at $Pr = 1, 2$, the turbulent Prandtl number approaches a constant value of 1.07 closer to the wall. It appears that the turbulent Prandtl number close to the wall is independent of the molecular Prandtl number, as shown in the studies by Li *et al.* (2009). This independence of the turbulent Prandtl number at the wall with respect to the molecular Prandtl number has also been reported in many other studies like Kong *et al.* (2000) and Jacobs & Durbin (2000) for TBL flow, as well as in Kim & Moin (1989) and Kasagi, Tomita & Kuroda (1992) for turbulent channel flow. However, from the present study, we find that the turbulent Prandtl number indeed depends on the molecular Prandtl number and this observation is based on the increasing value of Pr_t at the wall with respect to the scalars with $Pr = 4, 6$, as shown in figure 13.

In order to verify the plausibility of the present observations at $Pr = 4, 6$, the obtained DNS data were compared with the DNS channel data reported by Alcántara-Ávila & Hoyas (2021). Figure 15 shows the comparison of Pr_t at different molecular Prandtl numbers, where the present DNS data were at $Re_\theta = 1070$, corresponding to $Re_\tau = 395$, and the data from Alcántara-Ávila & Hoyas (2021) were at $Re_\tau = 500$. Despite these differences, the turbulent Prandtl numbers close to the wall are in good agreement, confirming that the Pr-scaled wall-normal heat flux decreases with an increase in Pr for $Pr \gtrapprox 4$, as stated by Alcántara-Ávila & Hoyas (2021). Thus, the present observation confirms the constant behaviour of the turbulent Prandtl number very close to the wall and highlights its dependence on the molecular Prandtl number, which has been often ignored in turbulent heat-transfer calculations.

A brief discussion of the Reynolds-stress budget is provided in Appendix A.

3.5. *Higher-order statistics, shear stress and heat flux*

The higher-order statistics (specifically, the values of the third- and fourth-order moments of a quantity) provide information on the non-Gaussian behaviour of turbulence. The third- and fourth-order moments are also called the skewness and flatness, respectively, and for a statistically stationary variable m, they are defined as

$$\mathcal{S}(m) = \left\langle m^3 \right\rangle \Big/ \left\langle m^2 \right\rangle^{3/2}, \tag{3.20}$$

$$\mathcal{F}(m) = \left\langle m^4 \right\rangle \Big/ \left\langle m^2 \right\rangle^{2}. \tag{3.21}$$

The skewness and flatness of the streamwise and wall-normal velocity components are shown in figure 16 where, for the spanwise velocity, we observe a Gaussian behaviour in the overlap region, as expected. The higher-order moments obtained by Vreman & Kuerten (2014) for the turbulent channel flow are compared with the present TBL results at $Re_\tau = 180$ (corresponding to $Re_\theta = 420$), showing a reasonable agreement. From figure 2, it should be highlighted that $Re_\theta = 420$ is roughly at the beginning of the turbulent regime and the deviation of the profiles for $y^+ > 100$ as observed in figure 16 is due to the intermittent wake region which decays to the values for a Gaussian distribution as the free stream is approached. There are some differences observed in the overlap region where the skewness of u is roughly 10 % higher than that reported by Vreman & Kuerten (2014). Although the plots indicate an overall good agreement, some drastic differences are observed in the flatness of the wall-normal and spanwise velocity

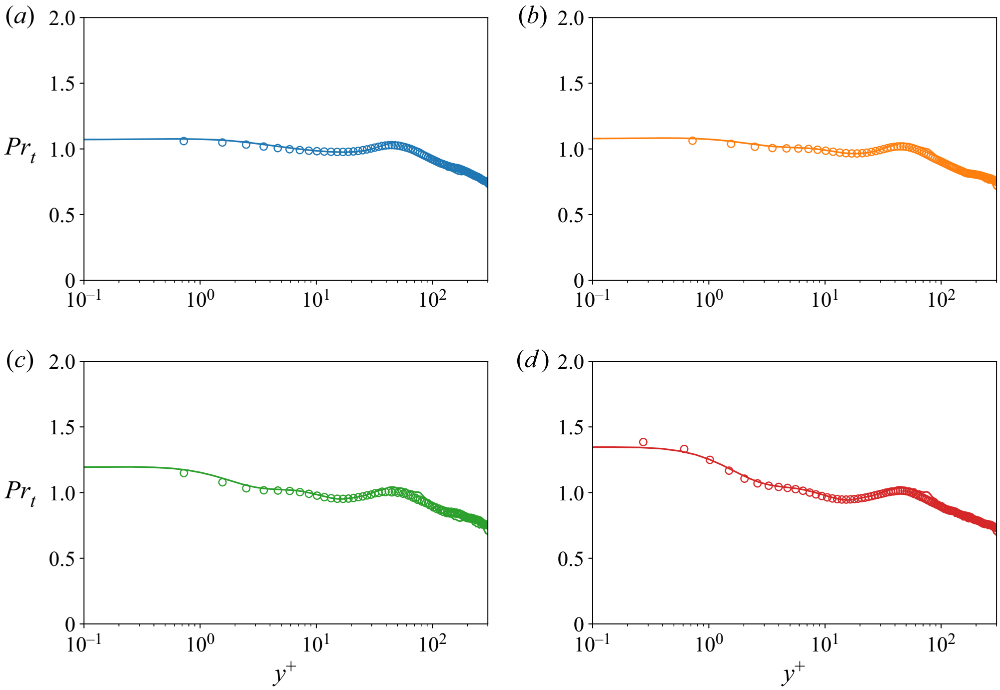

Figure 15. Comparison of turbulent Prandtl number against the channel DNS data at $Re_\theta = 1070$ for different molecular Prandtl numbers. Present DNS for (——, blue) $Pr = 1$, (——, orange) $Pr = 2$, (——, green) $Pr = 4$, (——, red) $Pr = 6$, channel DNS data by Alcántara-Ávila & Hoyas (2021) at $Re_\tau = 497$ and (○, blue) $Pr = 1$, (○, orange) $Pr = 2$, (○, green) $Pr = 4$, (○, red) $Pr = 6$.

components close to the wall, where the turbulence is highly intermittent. The flatness of the wall-normal velocity component approaches a value of ≈ 29 close to the wall for the data provided by Vreman & Kuerten (2014) whereas, in the TBL, it converges to ≈ 20. This is still lower than the value of 22 obtained by Kim, Moin & Moser (1987). The skewness of the pressure fluctuations is roughly 20 % higher in the overlap region of the TBL compared with the channel. Further, the intermittency (flatness) of the pressure is higher than the velocity components as reported by Kim *et al.* (1987), whereas the data obtained with TBL show an offset of 15 % throughout and are lower than the flatness behaviour observed in the channel. The flatness factor for pressure fluctuation at the wall approaches a value of 4.5 in the present simulations as compared with the values of 4.7 (Li *et al.* 2009) and 4.9 (Schewe 1983), whereas a value of ≈5.2 is reported by Vreman & Kuerten (2014).

The Reynolds shear stress is plotted in figure 17 and it is compared with the TBL data provided by Jiménez *et al.* (2010) and the channel DNS data by Kozuka *et al.* (2009). Even if there is a good agreement between the data in the inner region, there is a clear difference in the overlap region between the channel and the TBL. Such differences were also observed in the plots of the fluctuations in the streamwise and wall-normal directions shown in figure 8. The peak of the Reynolds shear stress is higher for the TBL compared with a channel flow, which indicates a higher momentum transfer by the fluctuating velocity field in the TBL. Looking at the energy budgets for shear stress component in both the channel and TBL corresponding to $Re_\tau = 395$ (plots not shown here), we find that there is higher production in the TBL compared with channel flows

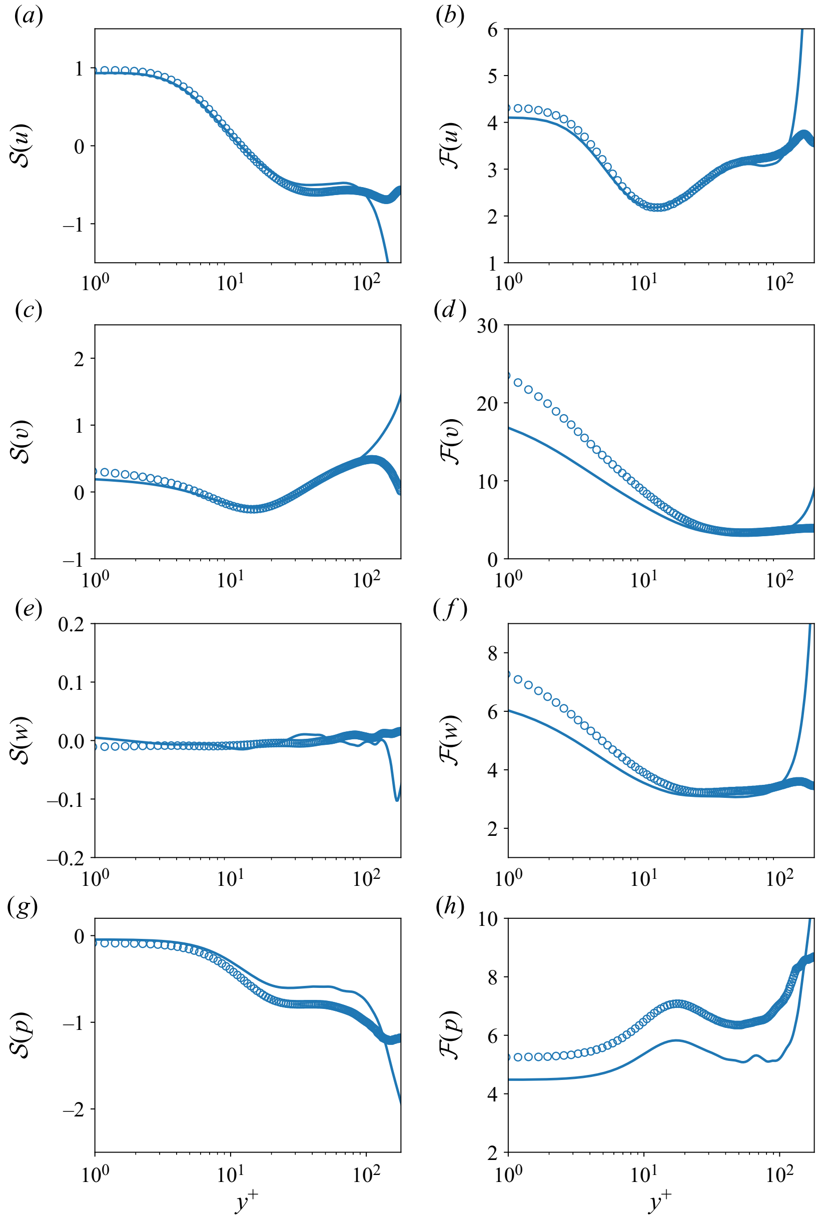

Figure 16. Skewness and flatness for the streamwise, wall-normal and spanwise velocity components at $Re_\theta = 420$ corresponding to $Re_\tau = 180$. (——, blue) Present DNS, (○, blue) channel DNS data by Vreman & Kuerten (2014) at $Re_\tau = 180$.

(with uniform-heat-flux wall conditions) in the overlap region whereas the dissipation was of similar magnitude.

The turbulent streamwise heat flux shows a reasonable agreement with the channel data available at $Pr = 1, 2$, as shown in figure 18, although the peaks for the channel-flow data are slightly higher and closer to the wall compared with the present observations. For $Pr = 4$, however, the peak of the streamwise heat flux is higher in the channel data by Alcántara-Ávila *et al.* (2018), since the heat flux is reported at a higher Reynolds number

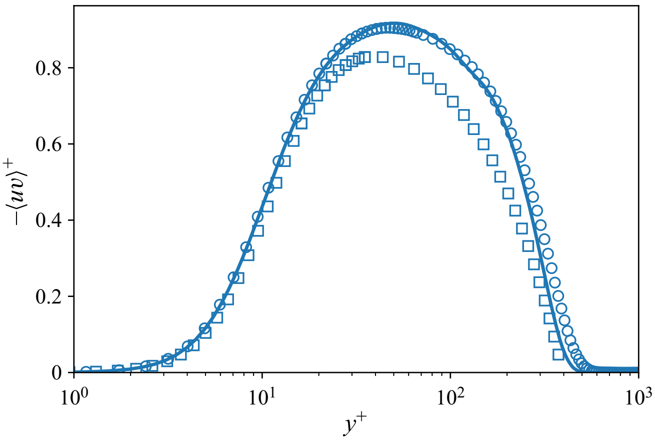

Figure 17. Inner-scaled Reynolds shear stress as a function of the wall-normal direction at $Re_\theta = 1070$. (——, blue) Present DNS, (○, blue) Jiménez *et al.* (2010) at $Re_\theta = 1100$, (□, blue) channel DNS data by Kozuka *et al.* (2009) at $Re_\tau = 395$.

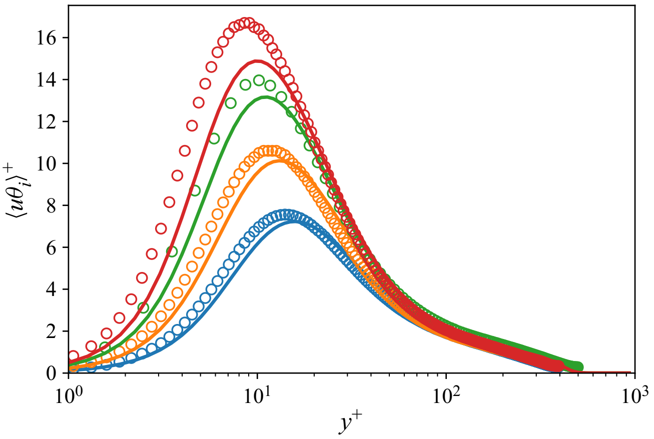

Figure 18. Variation of streamwise heat flux along the wall-normal direction at $Re_\theta = 1070$ for different passive scalars. Present DNS data for (——, blue) $Pr = 1$, (——, orange) $Pr = 2$, (——, green) $Pr = 4$, (——, red) $Pr = 6$, channel DNS data by Kozuka *et al.* (2009) at $Re_\tau = 395$ and (○, blue) $Pr = 1$, (○, orange) $Pr = 2$, (○, red) $Pr = 7$, (○, green) channel DNS data by Alcántara-Ávila *et al.* (2018) at $Re_\tau = 500$ and $Pr = 4$.

than our DNS. Furthermore, the comparison at the highest Pr in our simulation was at a slightly lower Pr than that in the channel and hence there is a difference in the slope of the streamwise heat flux close to the wall. Figure 19 shows the wall-normal heat flux for the different simulations. A clear difference can be observed in the outer region when comparing similar Prandtl numbers. On the other hand, the boundary-layer data and the channel data show a better agreement in the inner region.

The correlation coefficients provide more information on the statistical association between the fields, and here the structure of the flow field and scalar fluctuations are

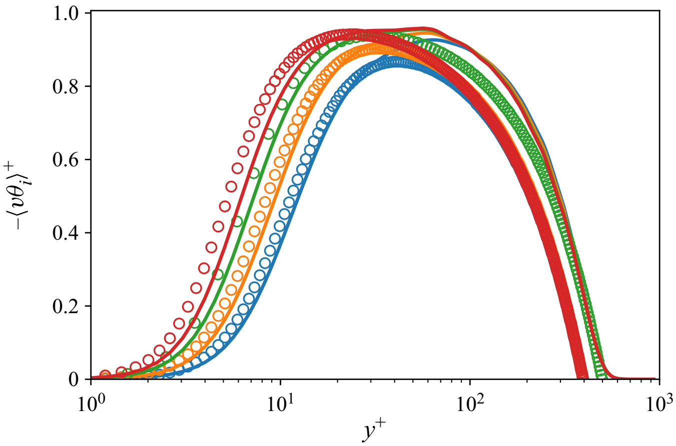

Figure 19. Variation of wall-normal heat flux along the wall-normal direction at $Re_\theta = 1070$ for different passive scalars. Present DNS data for (——, blue) $Pr = 1$, (——, orange) $Pr = 2$, (——, green) $Pr = 4$, (——, red) $Pr = 6$, channel DNS data by Kozuka *et al.* (2009) at $Re_\tau = 395$ and (○, blue) $Pr = 1$, (○, orange) $Pr = 2$, (○, red) $Pr = 7$, (○, green) channel DNS data by Alcántara-Ávila *et al.* (2018) at $Re_\tau = 500$ and $Pr = 4$.

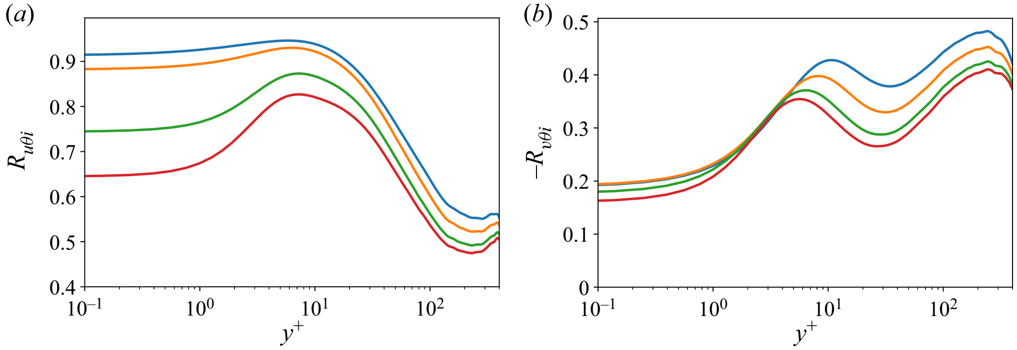

Figure 20. Correlation coefficients: (*a*) $u - \theta_i$, (*b*) $v - \theta_i$. Present DNS data for scalars at (——, blue) $Pr = 1$, (——, orange) $Pr = 2$, (——, green) $Pr = 4$, (——, red) $Pr = 6$ at $Re_\theta = 1070$.

analysed in terms of

$$\left.\begin{aligned} R_{u\theta_i} &= \frac{\langle u\theta_i \rangle}{u_{rms}\theta_{i\,rms}}, \\ R_{v\theta_i} &= \frac{\langle v\theta_i \rangle}{v_{rms}\theta_{i\,rms}}. \end{aligned}\right\} \tag{3.22}$$

The correlation-coefficient plot in figure 20 corresponding to $u - \theta_i$ shows a strong correlation of streamwise velocity and scalar fluctuations at $Pr = 1$ and it decreases with increase in Prandtl number. This is related to the similarity in the momentum and passive scalar transport by the turbulent eddies close to the wall. On the other hand, the $v - \theta_i$ correlation coefficient also shown in figure 20 exhibits an increasing trend with the Prandtl number. In the conductive sub-layer the correlation coefficients coincide for the various Prandtl numbers under study and then approach different values at the wall. This highlights a similar behaviour of the turbulent wall-normal momentum and passive scalar fields with a caveat, i.e. the differences are present very close to the wall for different Prandtl numbers.

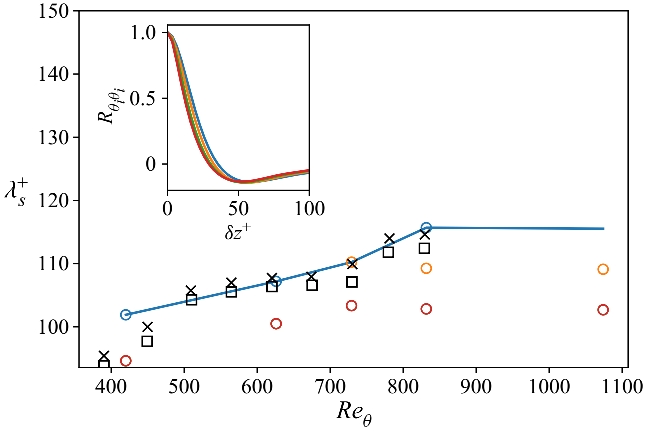

Figure 21. Variation of mean spanwise streak spacing along the streamwise direction at $y^+ \approx 7$. (——, blue) U, (○, blue) Θ_1, (○, orange) Θ_2, (○, green) Θ_3, (○, red) Θ_4. Comparison data from Li *et al.* (2009) for (×, black) U, (□, black) Θ_2. Inset: spanwise two-point correlation for (——, blue) Θ_1, (——, orange) Θ_2, (——, green) Θ_3, (——, red) Θ_4 at $Re_\theta \approx 830$.

3.6. *Spanwise two-point correlations*

The two-point correlations provide some quantitative information on the turbulent structures near the wall. For example, the streak spacing near the wall is of interest and can also be observed in an experimental setting. In order to identify the mean streak spacing, spanwise two-point correlations of the velocity components and passive scalars were obtained at five different positions along the streamwise direction at different wall-normal positions. Overall, the obtained results at $Re_\theta = 830$ were compared with the data reported by Kim *et al.* (1987) and show good agreement (not depicted here). The obtained two-point correlations for different scalars at $Re_\theta = 830$ are shown in figure 21 to assess the differences for varying Pr. The two-point correlation becomes negative and reaches a minimum at an inner-scaled correlation length of $\delta z^+ \approx 50$. The length at which the minimum occurs provides an estimate of the half-mean separation between the streaks in the spanwise direction, i.e. $(\lambda_s^+/2)$. The streak spacing is plotted along the streamwise direction at a wall-normal position of $y^+ \approx 7$, as shown in figure 21. Overall, the velocity and scalar streak spacings increase with Re_θ, as reported in the works of Li *et al.* (2009) and Schlatter *et al.* (2009). Note that the correlations are available only at five streamwise locations (solid line for U in figure 21 is for clarity), but the comparison with Li *et al.* (2009) is in reasonably good agreement for the velocity and scalar streaks at $Pr = 2$. The velocity streak spacing increases from 102 to 115 and appears to saturate for $Re_\theta > 830$. Note that such a saturation of streak spacing was also pointed out by Li *et al.* (2009) for $Re_\theta > 1500$. From figure 21, we also observe that the streak spacing decreases with increasing Pr and that the streak spacings for the scalars at $Pr = 4, 6$ are indistinguishable, although the rate of decay of the two-point correlations for the scalars is different. A higher grid resolution might be necessary to quantify the possible differences in the scalar streak spacing at higher Pr.

3.7. *Scaling of wall-heat-flux fields*

The wall-shear and heat-flux fields at different Prandtl numbers are normalized by subtracting the mean and dividing by the corresponding r.m.s. quantities.

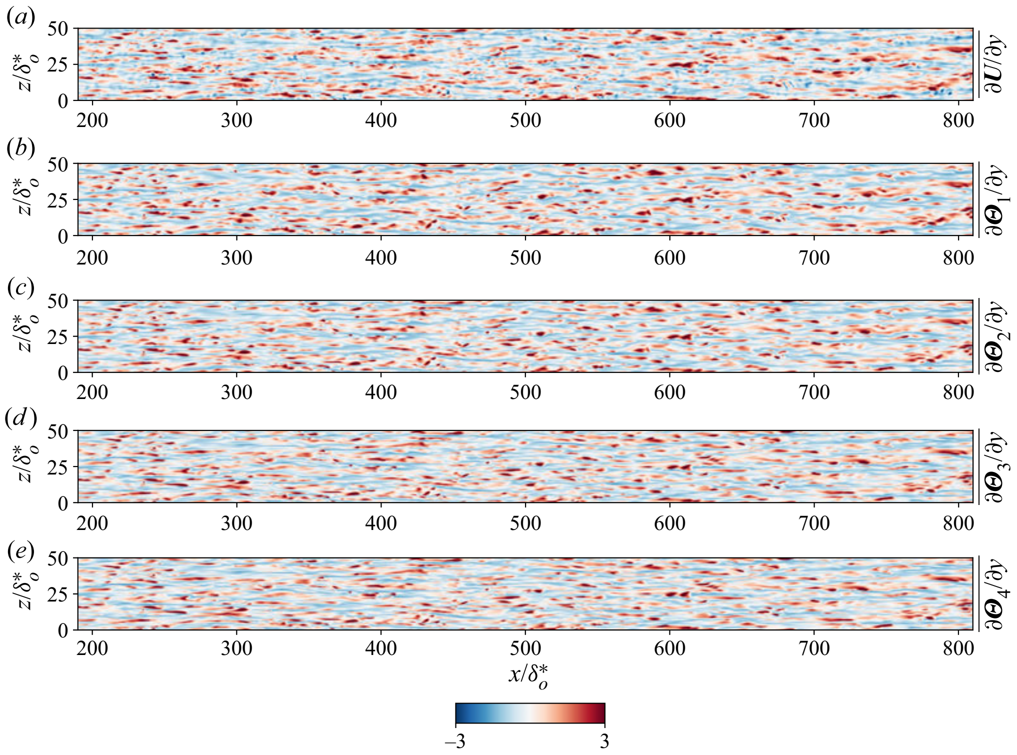

Figure 22. Instantaneous normalized streamwise wall-shear and heat-flux fields at different Prandtl numbers.

The normalization of a quantity n is calculated as

$$\bar{n} = \frac{n - \langle n \rangle}{n_{rms}}. \tag{3.23}$$

For the results discussed, n could indicate streamwise wall-shear stress, streamwise scalar flux, streamwise velocity or scalar concentrations at different Prandtl numbers. Figure 22 shows the instantaneous normalized streamwise wall-shear and heat-flux fields at different Prandtl numbers. The instantaneous normalized streamwise velocity and scalar fields are shown at $y^+ = 15$ (corresponding to $x/\delta_0^* = 500$) in figure 23. The normalized wall fields appear qualitatively similar and this result is confirmed by the distribution of the data in the streamwise shear and heat-flux fields obtained from 3700 samples, shown in figure 24. Although the distribution of data is different in the various fields, after normalization the distributions become identical. This indicates the uniformity in the distribution of the fluctuations of shear and heat flux when scaled with the corresponding r.m.s. quantities. This observation is useful for certain applications, for instance, in the prediction of fluctuating flow quantities from the wall, as discussed in the study by Guastoni *et al.* (2022).

4. Spectral analysis

The analysis of thermal boundary-layer statistics reveals that the scalar fluctuations and heat flux are strongly affected by the Prandtl number of the scalar in the flow and the corresponding scalings were reported in § 3. Additional insight can be obtained by

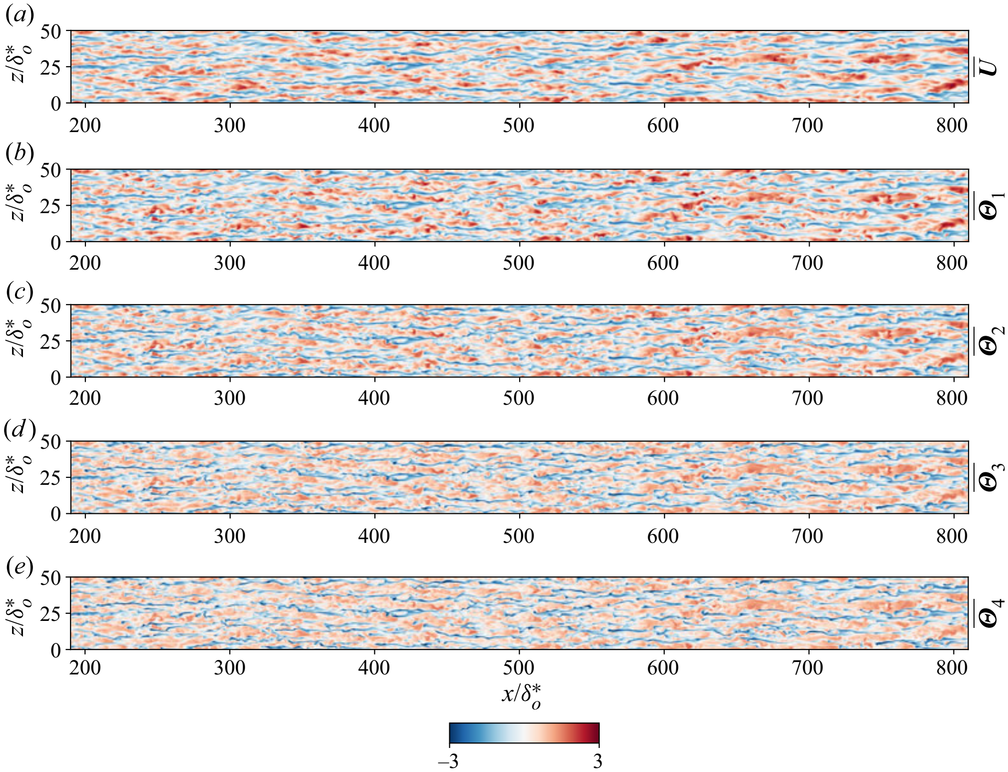

Figure 23. Instantaneous normalized streamwise velocity and passive scalar fields for different Prandtl numbers corresponding to $y^+ = 15$ at $x/\delta_0^* = 500$.

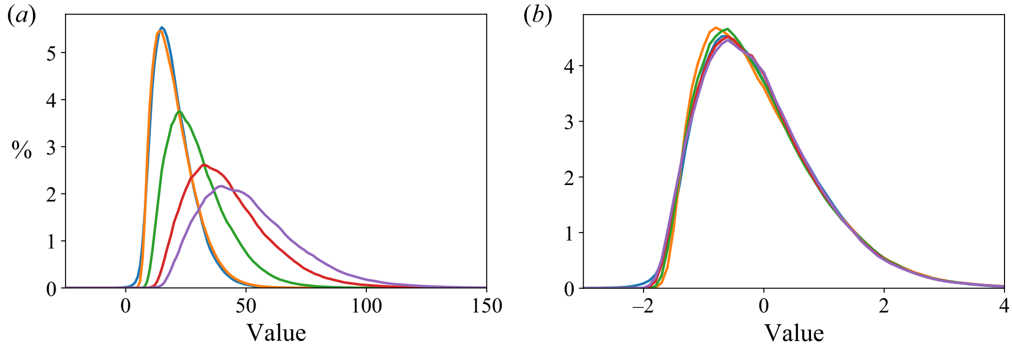

Figure 24. Probability density function of wall-shear and heat-flux fields at different Prandtl numbers. (*a*) Distribution of absolute data in the fields with a bin size of 1 unit, (*b*) distribution of the normalized data in the fields with a bin size of 0.1 unit, (——, blue) $\partial U/\partial y$ or $\overline{\partial U/\partial y}$, (——, orange) $\partial \Theta_1/\partial y$ or $\overline{\partial \Theta_1/\partial y}$, (——, green) $\partial \Theta_2/\partial y$ or $\overline{\partial \Theta_2/\partial y}$, (——, red) $\partial \Theta_3/\partial y$ or $\overline{\partial \Theta_3/\partial y}$, (——, purple) $\partial \Theta_4/\partial y$ or $\overline{\partial \Theta_4/\partial y}$.

analysing the energy distribution at the different length scales for the scalars at the simulated Prandtl numbers. In this regard, time series of the wall-shear, wall heat flux, streamwise velocity and different scalars were sampled at different wall-normal locations with a sampling time ($\sim\Delta t_s^+ = 1$ with the reference friction velocity at $x/\delta_0^* = 500$)

corresponding to 12 000 time units (δ_0^*/U_∞). The two-dimensional (2-D) premultiplied power-spectral density (PSD) $k_z k_t \phi(\lambda_z^+, \lambda_t^+)$ is obtained in the spanwise direction and in time based on the time series, for a total sampled time of about 11.5 flow-through times. Note that, here, $\boldsymbol{k_z}, \boldsymbol{k_t}$ denote the spanwise, temporal wavenumber, respectively, and ϕ is the PSD defined for the particular quantity under study.

For the calculation of PSD, the procedure outlined in Pozuelo *et al.* (2022) is utilized. After the mean subtraction of the sampled time series to obtain the turbulent quantities, first a 1-D spectrum $E[t, x](\lambda_z^+)$ is obtained by performing a fast Fourier transform (FFT) in the spanwise direction, due to the periodicity condition imposed along z. As a result, a spectral decomposition of the energy content into different wavenumbers k_z is obtained with the corresponding wavelengths λ_z given by $2\pi/k_z$. Note that the local friction velocity is used to obtain the inner-scaled quantities. It should be pointed out that the flow is developing along the streamwise direction and hence the FFT along the streamwise direction is not applicable. In the present spectral analysis, we consider the Re_θ range between 470 and 1070 and use Welch's overlapping-window method to address the non-periodicity in the temporal signal. As a next step, the spectrum in time is obtained using Welch's method with 15 bins in total, where 8 of them are independent. A Hamming window is used for imposing the periodicity in the bins, and the 2-D spectrum is obtained as $E[x](\lambda_z^+, \lambda_t^+)$ by using FFT along z and Welch's method in t, with λ_t denoting the temporal wavelength (i.e. the period), which is defined as $\lambda_t = 2\pi/k_t$. The obtained spectrum is divided by $\Delta k_t \Delta k_z$ and premultiplied with $k_t k_z$. Finally, an averaging along x is performed to yield the 2-D premultiplied PSD $k_t k_z \phi(\lambda_z^+, \lambda_t^+)$.

The 2-D PSDs of the streamwise wall shear and wall heat flux at different Prandtl numbers are provided in figure 25, along with the PSD of the streamwise velocity and scalar fluctuations at $y^+ = 15$. The obtained 2-D PSD at $y^+ = 15$ agrees well with the results reported by Pozuelo *et al.* (2022), although the latter are at higher Reynolds number. At the wall, the spectral peak is observed at $\lambda_z^+ \approx 100$ and $\lambda_t^+ \approx 100$. Furthermore, at $y^+ = 15$, we observe that the maximum of spectral-energy distribution is at $\lambda_z^+ \approx 120$, which corresponds to the characteristic streak spacing in wall turbulence (Smith & Metzler 1983). It is observed that the PSD for the streamwise wall-shear stress is very similar to that for the wall heat flux at $Pr = 1$, which is an expected result for the reasons outlined in § 3.1. However, with increasing Pr, the PSD shifts to the right, indicating that the energy is not spread over a wider range of scales, and instead is concentrated in longer temporal structures. One could argue that, with a shorter boundary layer, the structures at $Pr = 6$ can become larger than the ones developing at $Pr = 1$. Because of this, the larger structures have a different footprint at the wall. Additionally, the plots in figure 25 also exhibit a slight trend downwards for higher Pr, a fact that indicates the presence of smaller spanwise scales, in agreement with the discussion in § 3.6. Overall, the temporal wavelength range at which we have the most energetic structures in the wall-heat-flux fields increases for larger Prandtl numbers. From the above observations, considering the dominant energetic structures to be composed of streaks at the wall, the scalar at $Pr = 6$ (in general for higher Pr) might exhibit longer and thinner scalar streak structures at the wall compared with the case at $Pr = 1$.

The PSDs calculated at $y^+ = 30$ and 50 are shown in figure 26. From this figure, we observe that the similarity in the distribution of energy for the scalar at $Pr = 1$ and the streamwise velocity is lost as we move farther from the wall. In contrast to the observation of large streamwise structures at the wall, we find an increasing concentration of energy in smaller scales as we increase the Prandtl number. Further, the range of scales in which

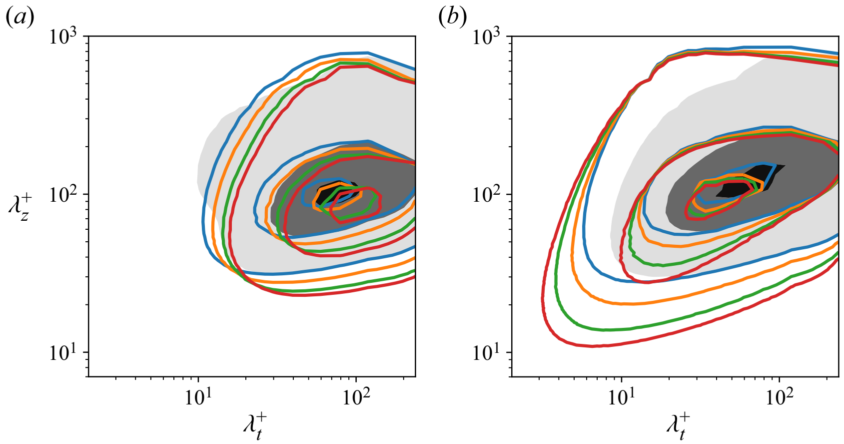

Figure 25. Two-dimensional premultiplied PSD of (*a*) streamwise wall-shear and wall-heat-flux fields and (*b*) streamwise velocity and scalar at $y^+ = 15$, for the ZPG thermal TBL with Re_θ ranging from 467 to 1072. The three contour lines correspond to 10 %, 50 % and 90 % of the maximum energy density. We show: $k_t k_z \phi_{u_y u_y}$ or $k_t k_z \phi_{uu}$ (shaded contours), (——, blue) $k_t k_z \phi_{\Theta_{1y} \Theta_{1y}}$ or $k_t k_z \phi_{\Theta_1 \Theta_1}$, (——, orange) $k_t k_z \phi_{\Theta_{2y} \Theta_{2y}}$ or $k_t k_z \phi_{\Theta_2 \Theta_2}$, (——, green) $k_t k_z \phi_{\Theta_{3y} \Theta_{3y}}$ or $k_t k_z \phi_{\Theta_3 \Theta_3}$, (——, red) $k_t k_z \phi_{\Theta_{4y} \Theta_{4y}}$ or $k_t k_z \phi_{\Theta_4 \Theta_4}$, correspondingly. Here, the spatial coordinate in subscript denotes partial derivative with respect to that coordinate. Panels show (*a*) $y^+ = 0$, (*b*) $y^+ = 15$.

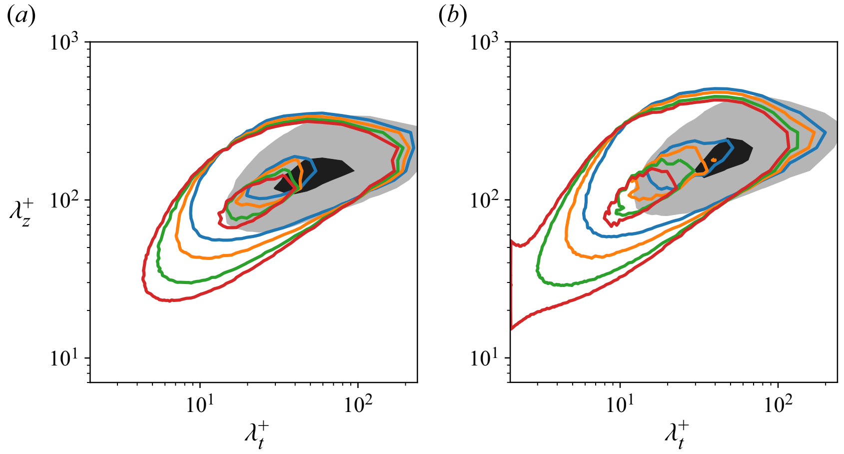

Figure 26. Two-dimensional premultiplied PSD of streamwise velocity and scalar fields at (*a*) $y^+ = 30$ and (*b*) $y^+ = 50$. The two contour lines correspond to 10 % and 50 % of the maximum energy density. We show: $k_t k_z \phi_{uu}$ (shaded contours), (——, blue) $k_t k_z \phi_{\Theta_1 \Theta_1}$, (——, orange) $k_t k_z \phi_{\Theta_2 \Theta_2}$, (——, green) $k_t k_z \phi_{\Theta_3 \Theta_3}$, (——, red) $k_t k_z \phi_{\Theta_4 \Theta_4}$.

the energy is distributed also increases with *Pr*. Focusing on the most energetic structures, we find that these are concentrated in a region of smaller temporal and spanwise scales with increasing *Pr* at both $y^+ = 30$ and 50. For the scalar at $Pr = 6$, the spectral peak is observed at $\lambda_z^+ \approx 100$ and $\lambda_t^+ \approx 20$ for $y^+ = 30$ and 50.

5. Summary and conclusions

In the present study, a DNS of the thermal TBL is performed up to $Re_\theta = 1080$ with passive scalars at $Pr = 1, 2, 4$ and 6, which to authors' knowledge is the highest Prandtl number simulated for the thermal boundary layer. Various statistical quantities for the flow and scalars were computed and compared against the reported channel and TBL data in the literature. Overall, the statistical quantities are in good agreement with the existing data whenever a comparison is possible. For higher Pr, we also observed that the peak of the scalar fluctuations decreases when Re_τ increases, which is different from the trend reported in the literature. Further, we showed that the variation of the peak in scalar fluctuation has a weak dependence with Re_τ compared with the Prandtl number. Similarly, the peak in the heat flux also exhibits a weak dependence with Re_τ compared with Pr of the scalar and the heat flux scales as $\sim Pr^{0.4}$.

In the present study, we also highlighted the behaviour of the turbulent Prandtl number Pr_t, which does not approach a constant value of 1.07 as the wall is approached for higher Prandtl numbers. In addition, we also found the corresponding Pr_t to increase with Pr, confirming the findings of Alcántara-Ávila & Hoyas (2021). Finally, a brief description of the energy distribution in the scales for different Pr at different wall-normal locations is presented by analysing the 2-D pre-multiplied PSD.

The analysis and data provided in this work are expected to serve as a database for the research community to assess the validity of new turbulence models and validate other numerical and experimental results.

Acknowledgements. The simulations were run with the computational resources provided by the Swedish National Infrastructure for Computing (SNIC). The authors of the various databases used in this study are acknowledged for sharing the simulation data.

Funding. This work is supported by the funding provided by the Swedish e-Science Research Centre (SeRC), ERC grant no. '2021-CoG-101043998, DEEPCONTROL' to RV and the Knut and Alice Wallenberg (KAW) Foundation.

Declaration of interests. The authors report no conflict of interest.

Data availability statement. The data that support the findings of this study are available on GitHub– KTH-Flow-AI.

Author ORCIDs.
Arivazhagan G. Balasubramanian https://orcid.org/0000-0002-0906-3687;
Luca Guastoni https://orcid.org/0000-0002-8589-1572;
Philipp Schlatter https://orcid.org/0000-0001-9627-5903;
Ricardo Vinuesa https://orcid.org/0000-0001-6570-5499.

Appendix A. Reynolds-stress budget

The Reynolds-stress equation is written (in index notation) as

$$\frac{\mathrm{D}\langle u_j u_k \rangle}{\mathrm{D}t} = \mathcal{P}_{jk} - \epsilon_{jk} + C_{jk} + \mathcal{D}_{jk} + T_{jk}, \tag{A1}$$

where $\mathrm{D}/\mathrm{D}t$ represents the material derivative and $\langle u_j u_k \rangle$ is the Reynolds-stress tensor. Here, $\mathcal{P}_{jk}$ denotes the production term, ϵ_{jk} is the viscous dissipation rate tensor, C_{jk} is the velocity pressure-gradient term (which can be split into the pressure strain term and pressure diffusion term), T_{jk} is the turbulent diffusion and $\mathcal{D}_{jk}$ is the molecular

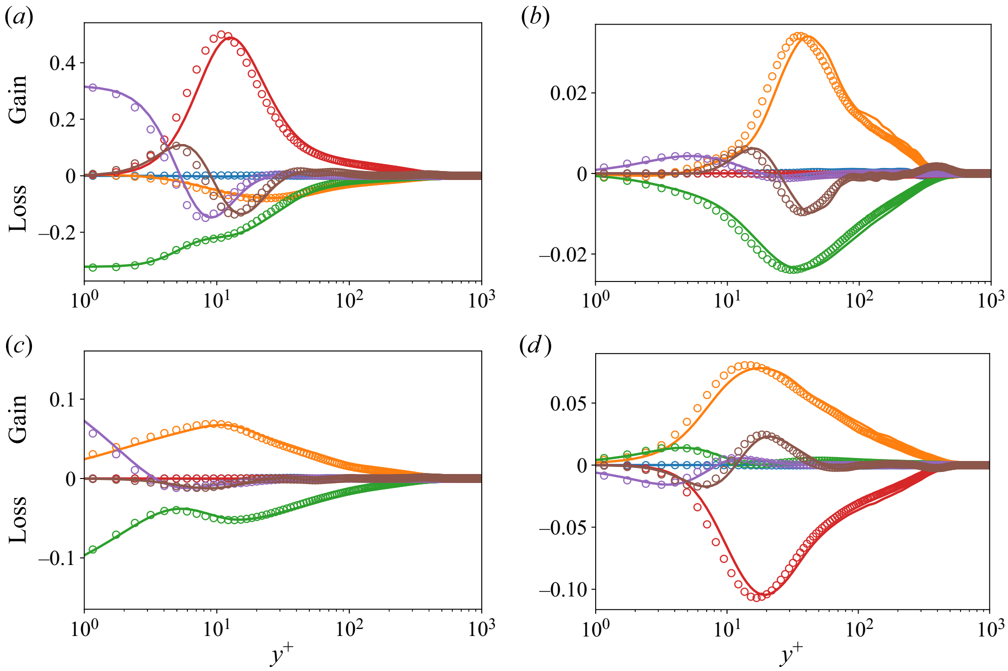

Figure 27. Comparison of the Reynolds-stress budgets; (*a*) $\langle uu \rangle$, (*b*) $\langle vv \rangle$, (*c*) $\langle ww \rangle$, (*d*) $\langle uv \rangle$, (——, black) present DNS, (○, black) Jiménez *et al.* (2010), (——, blue) convection, (——, orange) velocity-pressure diffusion, (——, green) dissipation, (——, red) production, (——, purple) molecular diffusion, (——, brown) turbulent diffusion.

diffusion term. The corresponding terms are written respectively as

$$\mathcal{P}_{jk} := -\langle u_k u_l \rangle \frac{\partial \langle U_j \rangle}{\partial x_l} - \langle u_j u_l \rangle \frac{\partial \langle U_k \rangle}{\partial x_l}, \tag{A2}$$

$$\epsilon_{jk} := 2\nu \left\langle \frac{\partial u_j}{\partial x_l} \frac{\partial u_k}{\partial x_l} \right\rangle, \tag{A3}$$

$$C_{jk} := -\frac{1}{\rho} \left\langle u_j \frac{\partial p}{\partial x_k} + u_k \frac{\partial p}{\partial x_j} \right\rangle, \tag{A4}$$

$$T_{jk} := -\frac{\partial}{\partial x_l} \langle u_j u_k u_l \rangle, \tag{A5}$$

$$\mathcal{D}_{jk} := \nu \frac{\partial^2}{\partial x_l \partial x_l} \langle u_j u_k \rangle . \tag{A6}$$

A detailed description of the above terms can be found in Pope (2000) and they are non-dimensionalized by u_τ^4/ν.

The obtained Reynolds-stress budgets at $Re_\theta = 1080$ (which is located almost at the end of the computational domain before the fringe region) are compared with the data by Jiménez *et al.* (2010) in the TBL at $Re_\theta = 1100$, as shown in figure 27. All the different components contributing to the stress terms are in good agreement with the reference data.

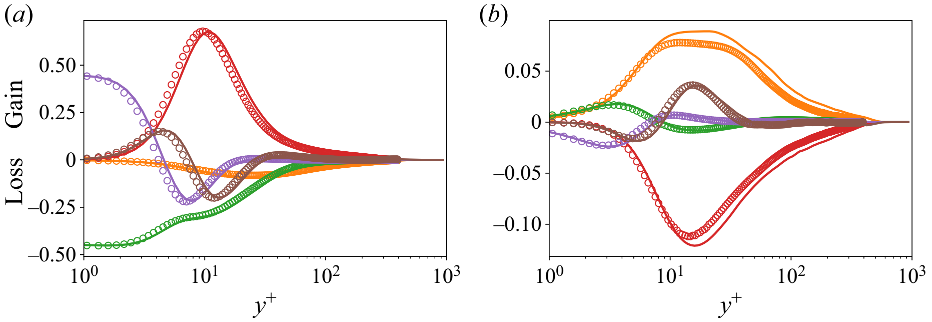

Figure 28. Comparison of the scalar-flux budgets; (*a*) $\langle u\theta_i\rangle$, (*b*) $\langle v\theta_i\rangle$, (——, black) present DNS at $Pr = 2$, (○, black) Kozuka *et al.* (2009) at $Pr = 2$, (——, blue) convection, (——, orange) scalar-pressure diffusion, (——, green) dissipation, (——, red) production, (——, purple) molecular diffusion, (——, brown) turbulent diffusion.

The scalar-flux equation is written (in index notation) as

$$\frac{\mathrm{D}\left\langle u_j\Theta_i\right\rangle}{\mathrm{D}t} = \mathcal{P}_{\Theta_{ij}} - \epsilon_{\Theta_{ij}} + C_{\Theta_{ij}} + \mathcal{D}_{\Theta_{ij}} + T_{\Theta_{ij}}, \tag{A7}$$

where $\mathcal{P}_{\Theta_{ij}}$ is the production term due to both the mean gradients of the velocity and scalar Θ_i, $\epsilon_{\Theta_{ij}}$ is the dissipation term, $C_{\Theta_{ij}}$ is the scalar-pressure-gradient correlation term (which can be split into a pressure scalar-gradient correlation term and a divergence of the pressure–scalar correlation term), $T_{\Theta_{ij}}$ is the turbulent diffusion and $\mathcal{D}_{\Theta_{ij}}$ is the molecular diffusion term. The terms are defined as

$$\mathcal{P}_{\Theta_{ij}} := -\left\langle u_l\theta_i\right\rangle \frac{\partial\left\langle U_j\right\rangle}{\partial x_l} + \left\langle u_j u_l\right\rangle \frac{\partial\left\langle\Theta_i\right\rangle}{\partial x_l}, \tag{A8}$$

$$\epsilon_{\Theta_{ij}} := \left(\nu + \frac{k}{\rho C_p}\right)\left\langle \frac{\partial u_j}{\partial x_l}\frac{\partial\theta_i}{\partial x_l}\right\rangle, \tag{A9}$$

$$C_{\Theta_{ij}} := -\frac{1}{\rho}\left(\frac{\partial\left\langle p\theta_i\right\rangle}{\partial x_j} - \left\langle p\frac{\partial\theta_i}{\partial x_j}\right\rangle\right), \tag{A10}$$

$$T_{\Theta_{ij}} := -\frac{\partial}{\partial x_l}\left\langle u_j u_l\theta_i\right\rangle, \tag{A11}$$

$$\mathcal{D}_{\Theta_{ij}} := \frac{\partial}{\partial x_l}\left(\frac{k}{\rho C_p}\left\langle u_j\frac{\partial\theta_i}{\partial x_l}\right\rangle + \nu\left\langle\theta_i\frac{\partial u_j}{\partial x_l}\right\rangle\right). \tag{A12}$$

A detailed description of the scalar-flux budget terms can be found in Kozuka *et al.* (2009) and Li *et al.* (2009). Due to the lack of TBL data at higher Prandtl numbers, the budgets for the scalar at $Pr = 2$ are compared against the channel DNS data from Kozuka *et al.* (2009), as shown in figure 28. Overall, there is a good comparison obtained for the different terms in the scalar-flux budgets. Also, as discussed in § 3.5, we observe a higher production compared with the channel-flow case for the vertical passive scalar-flux budget in the overlap region. In addition, the scalar-pressure diffusion term also exhibits the same behaviour as discussed above and it should be noted that the discrepancy not only stems from the different problem set-up but also the wall boundary condition for the scalar, which is Dirichlet in the present study and Neumann in the works

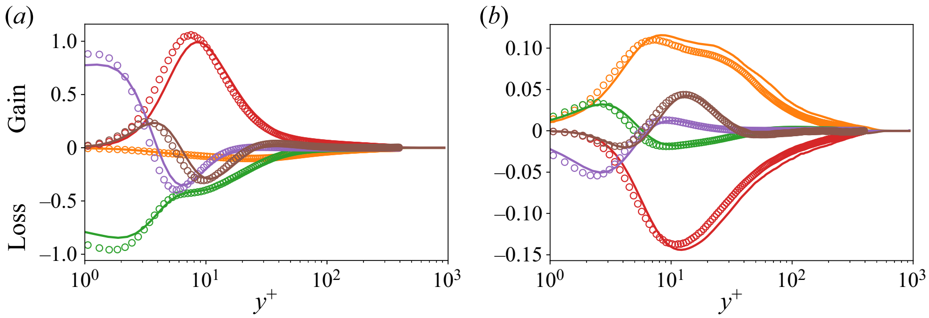

Figure 29. Comparison of the scalar-flux budgets; (*a*) $\langle u\theta_i \rangle$, (*b*) $\langle v\theta_i \rangle$, (——, black) present DNS at $Pr = 6$, (○, black) Kozuka *et al.* (2009) at $Pr = 7$, (——, blue) convection, (——, orange) scalar-pressure diffusion, (——, green) dissipation, (——, red) production, (——, purple) molecular diffusion, (——, brown) turbulent diffusion.

of Kozuka *et al.* (2009). Further, a comparison of the data obtained at $Pr = 6$ with the data obtained by Kozuka *et al.* (2009) at $Pr = 7$ for a channel flow is also provided in figure 29. Overall, the comparison of the stress budgets at different parameter points shows a good agreement with the data available in the literature. Note that the small discrepancy observed in figure 29 is due to the different Prandtl numbers.

REFERENCES

ABE, H., KAWAMURA, H. & MATSUO, Y. 2004 Surface heat-flux fluctuations in a turbulent channel flow up to $Re_\tau = 1020$ with $Pr = 0.025$ and 0.71. *Intl. J. Heat Fluid Flow* **25** (3), 404–419.

ALCÁNTARA-ÁVILA, F. & HOYAS, S. 2021 Direct numerical simulation of thermal channel flow for medium–high Prandtl numbers up to $Re_\tau = 2000$. *Intl J. Heat Mass Transfer* **176**, 121412.

ALCÁNTARA-ÁVILA, F., HOYAS, S. & PÉREZ-QUILES, M.J. 2018 DNS of thermal channel flow up to $Re_\tau = 2000$ for medium to low Prandtl numbers. *Intl J. Heat Mass Transfer* **127**, 349–361.

ALCÁNTARA-ÁVILA, F., HOYAS, S. & PÉREZ-QUILES, M.J. 2021 Direct numerical simulation of thermal channel flow for $Re_\tau = 5000$ and $Pr = 0.71$. *J. Fluid Mech.* **916**, A29.

ANTONIA, R.A. 1980 Behaviour of the turbulent Prandtl number near the wall. *Intl J. Heat Mass Transfer* **23**, 906–908.

ARAYA, G. & CASTILLO, L. 2012 DNS of turbulent thermal boundary layers up to $Re_\theta = 2300$. *Intl J. Heat Mass Transfer* **55** (15–16), 4003–4019.

BAILEY, S.C.C., *et al.* 2013 Obtaining accurate mean velocity measurements in high Reynolds number turbulent boundary layers using Pitot tubes. *J. Fluid Mech.* **715**, 642–670.

BATCHELOR, G.K. 1959 Small-scale variation of convected quantities like temperature in turbulent fluid. Part 1. General discussion and the case of small conductivity. *J. Fluid Mech.* **5** (1), 113–133.

BELL, D.M. & FERZIGER, J.H. 1993 Turbulent boundary layer DNS with passive scalars. In *Near-Wall Turbulent Flows* (ed. R.M.C. So, C.G. Speziale & B.E. Launder), pp. 327–336. Elsevier Science.

BERTOLOTTI, F.P., HERBERT, T. & SPALART, P.R. 1992 Linear and nonlinear stability of the Blasius boundary layer. *J. Fluid Mech.* **242**, 441–474.

BLOM, J. 1970 An experimental determination of the turbulent Prandtl number in a developing temperature boundary layer. PhD thesis, Technical University of Eindhoven.

BOUSSINESQ, J. 1877 Essai sur la théorie des eaux courantes. *Mem. Savants Etrangers Acad. Sci. Paris* **26**, 1–680.

CHANDRASEKHAR, S. 1961 *Hydrodynamic and Hydromagnetic Stability*. Oxford University Press.

CHEVALIER, M., SCHLATTER, P., LUNDBLADH, A. & HENNINGSON, D.S. 2007 SIMSON : a pseudo-spectral solver for incompressible boundary layer flows. *Tech. Rep.* TRITA-MEK 2007:07. KTH Mechanics, Stockholm, Sweden.

ERM, L.P. & JOUBERT, P.N. 1991 Low-Reynolds-number turbulent boundary layers. *J. Fluid Mech.* **230**, 1–44.

FERRANTE, A. & ELGHOBASHI, S. 2005 Reynolds number effect on drag reduction in a microbubble-laden spatially developing turbulent boundary layer. *J. Fluid Mech.* **543**, 93–106.

GUASTONI, L., BALASUBRAMANIAN, A.G., GÜEMES, A., IANIRO, A., DISCETTI, S., SCHLATTER, P., AZIZPOUR, H. & VINUESA, R. 2022 Non-intrusive sensing in turbulent boundary layers via deep fully-convolutional neural networks. Preprint, arXiv:2208.06024.

HATTORI, H., HOURA, T. & NAGANO, Y. 2007 Direct numerical simulation of stable and unstable turbulent thermal boundary layers. *Intl J. Heat Fluid Flow* **28** (6), 1262–1271.

HOLLINGSWORTH, D.K. JR. 1989 Measurement and prediction of the turbulent thermal boundary layer in water on flat and concave surfaces. PhD thesis, Stanford University.

JACOBS, R.G. & DURBIN, P.A. 2000 Bypass transition phenomena studies by computer simulation. *Tech. Rep.* Report no. TF-77. Mech. Eng. Dept., Stanford University.

JIMÉNEZ, J., HOYAS, S., SIMENS, M.P. & MIZUNO, Y. 2010 Turbulent boundary layers and channels at moderate Reynolds numbers. *J. Fluid Mech.* **657**, 335–360.

KADER, B.A. 1981 Temperature and concentration profiles in fully turbulent boundary layers. *Intl J. Heat Mass Transfer* **24** (9), 1541–1544.

KASAGI, N. & IIDA, O. 1999 Progress in direct numerical simulation of turbulent heat transfer. In *Proc. Fifth ASME/JSME Joint Thermal Engg. Conf.* (ed. D.L. Dwoyer & M.Y. Hussaini), pp. 15–19. Springer.

KASAGI, N., TOMITA, Y. & KURODA, A. 1992 Direct numerical simulation of passive scalar field in a turbulent channel flow. *Trans. ASME J. Heat Transfer* **114** (3), 598–606.

KAWAMURA, H., ABE, H. & MATSUO, Y. 1999 DNS of turbulent heat transfer in channel flow with respect to Reynolds and Prandtl number effects. *Intl J. Heat Fluid Flow* **20** (3), 196–207.

KAWAMURA, H., ABE, H. & SHINGAI, K. 2000 DNS of turbulence and heat transport in a channel flow with different Reynolds and Prandtl numbers and boundary conditions. In *Proc. Third Int. Symp. on Turbulence, Heat and Mass Transfer* (ed. Y. Nagano), pp. 15–32. Engineering Foundation.

KAYS, W.M. 1972 Heat transfer to the transpired turbulent boundary layer. *Intl J. Heat Mass Transfer* **15** (5), 1023–1044.

KAYS, W.M. 1994 Turbulent Prandtl number. Where are we? *Trans. ASME J. Heat Transfer* **116** (2), 284–295.

KAYS, W.M. & CRAWFORD, M.E. 1993 *Convective Heat and Mass Transfer*. McGraw-Hill.

KESTIN, J. & RICHARDSON, P.D. 1963 Heat transfer across turbulent, incompressible boundary layers. *Intl J. Heat Mass Transfer* **6** (2), 147–189.

KIM, J. & MOIN, P. 1989 Transport of passive scalars in a turbulent channel flow. In *Turbulent Shear Flows*, vol. 6 (ed. J.C. Andre *et al.*), pp. 85–96. Springer.

KIM, J., MOIN, P. & MOSER, R. 1987 Turbulence statistics in fully developed channel flow at low Reynolds number. *J. Fluid Mech.* **177**, 133–166.

KOMMINAHO, J. & SKOTE, M. 2002 Reynolds stress budgets in Couette and boundary layer flows. *Flow Turbul. Combust.* **68** (2), 167–192.

KONG, H., CHOI, H. & LEE, J.S. 2000 Direct numerical simulation of turbulent thermal boundary layers. *Phys. Fluids* **12** (10), 2555–2568.

KOZUKA, M., SEKI, Y. & KAWAMURA, H. 2009 DNS of turbulent heat transfer in a channel flow with a high spatial resolution. *Intl J. Heat Fluid Flow* **30** (3), 514–524.

KRISHNAMOORTHY, L.V. & ANTONIA, R.A. 1987 Temperature-dissipation measurements in a turbulent boundary layer. *J. Fluid Mech.* **176**, 265–281.

LAZPITA, E., MARTÍNEZ-SÁNCHEZ, Á., CORROCHANO, A., HOYAS, S., LE CLAINCHE, S. & VINUESA, R. 2022 On the generation and destruction mechanisms of arch vortices in urban fluid flows. *Phys. Fluids* **34** (5), 051702.

LI, Q. 2007 Direct numerical simulation of a turbulent boundary layer with passive scalar transport. *Tech. Rep.* KTH Royal Institute of Technology.

LI, Q., SCHLATTER, P., BRANDT, L. & HENNINGSON, D.S. 2009 DNS of a spatially developing turbulent boundary layer with passive scalar transport. *Intl J. Heat Fluid Flow* **30** (5), 916–929.

LIENHARD, J.H. 2020 Heat transfer in flat-plate boundary layers: a correlation for laminar, transitional, and turbulent flow. *Trans. ASME J. Heat Transfer* **142** (6), 061805.

LIENHARD, I.V. & JOHN, H. 2005 *A Heat Transfer Textbook*. Phlogiston Press.

LUND, T.S., WU, X. & SQUIRES, K.D. 1998 Generation of turbulent inflow data for spatially-developing boundary layer simulations. *J. Comput. Phys.* **140** (2), 233–258.

LUNDBLADH, A., BERLIN, S., SKOTE, M., HILDINGS, C., CHOI, J., KIM, J. & HENNINGSON, D.S. 1999 An efficient spectral method for simulation of incompressible flow over a flat plate. *Tech. Rep.* KTH/MEK/TR–99/11–SE. KTH Mechanics, Stockholm, Sweden.

MONIN, A.S. & YAGLOM, A.M. 1971 *Statistical Fluid Mechanics: Mechanics of Turbulence*, vol. 1. MIT Press.

NORDSTRÖM, J., NORDIN, N. & HENNINGSON, D.S. 1999 The fringe region technique and the Fourier method used in the direct numerical simulation of spatially evolving viscous flows. *SIAM J. Sci. Comput.* **20** (4), 1365–1393.

Örlü, R. & Alfredsson, P.H. 2010 On spatial resolution issues related to time-averaged quantities using hot-wire anemometry. *Exp. Fluids* **49** (1), 101–110.

Österlund, J.M. 1999 Experimental studies of zero pressure-gradient turbulent boundary layer flow. PhD thesis, KTH Royal Institute of Technology, Stockholm, Sweden.

Perry, A.E. & Hoffmann, P.H. 1976 An experimental study of turbulent convective heat transfer from a flat plate. *J. Fluid Mech.* **77** (2), 355–368.

Pirozzoli, S. 2023 An explicit representation for mean profiles and fluxes in forced passive scalar convection. *J. Fluid Mech.* **968**, R1.

Pirozzoli, S., Bernardini, M. & Orlandi, P. 2016 Passive scalars in turbulent channel flow at high Reynolds number. *J. Fluid Mech.* **788**, 614–639.

Pope, S.B. 2000 *Turbulent Flows*. Cambridge University Press.

Pozuelo, R., Li, Q., Schlatter, P. & Vinuesa, R. 2022 An adverse-pressure-gradient turbulent boundary layer with nearly constant $\beta \simeq 1.4$ up to $Re_\theta \simeq 8700$. *J. Fluid Mech.* **939**, A34.

Purtell, L.P., Klebanoff, P.S. & Buckley, F.T. 1981 Turbulent boundary layer at low Reynolds number. *Phys. Fluids* **24** (5), 802–811.

Rahgozar, S., Maciel, Y. & Schlatter, P. 2013 Spatial resolution analysis of planar PIV measurements to characterise vortices in turbulent flows. *J. Turbul.* **14** (10), 37–66.

Reynolds, O. 1874 On the extent and action of the heating surface for steam boilers. *Manchester Lit. Phil. Soc. Mem. Proc.* **14**, 7–12.

Roach, P.E. & Brierly, D.H. 1992 The influence of a turbulent free-stream on zero pressure gradient transitional boundary layer development: Part 1. Test cases T3A and T3B. In *Numerical Simulation of Unsteady Flows and Transition to Turbulence* (ed. O. Pironneau, W. Rodi, I.L. Rhyming, A.M. Savill & T.V. Truong), pp. 319–347. Cambridge University Press.

Samie, M., Marusic, I., Hutchins, N., Fu, M.K., Fan, Y., Hultmark, M. & Smits, A.J. 2018 Fully resolved measurements of turbulent boundary layer flows up to $Re_\tau = 20\,000$. *J. Fluid Mech.* **851**, 391–415.

Schewe, G. 1983 On the structure and resolution of wall-pressure fluctuations associated with turbulent boundary-layer flow. *J. Fluid Mech.* **134**, 311–328.

Schlatter, P., Örlü, R., Li, Q., Brethouwer, G., Fransson, J.H.M., Johansson, A.V., Alfredsson, P.H. & Henningson, D.S. 2009 Turbulent boundary layers up to $Re_\theta = 2500$ studied through simulation and experiment. *Phys. Fluids* **21** (5), 051702.

Schlatter, P., Li, Q., Brethouwer, G., Johansson, A.V. & Henningson, D.S. 2010 Simulations of spatially evolving turbulent boundary layers up to $Re_\theta = 4300$. *Intl J. Heat Fluid Flow* **31** (3), 251–261.

Schoenherr, K.E. 1932 Resistance of flat surfaces moving through a fluid. *Trans. Soc. Nav. Archit. Mar. Engrs* **40**, 279–313.

Schwertfirm, F. & Manhart, M. 2007 DNS of passive scalar transport in turbulent channel flow at high Schmidt numbers. *Intl J. Heat Fluid Flow* **28** (6), 1204–1214.

Shehzad, M., Sun, B., Jovic, D., Ostovan, Y., Cuvier, C., Foucaut, J.M., Willert, C., Atkinson, C. & Soria, J. 2021 Investigation of large scale motions in zero and adverse pressure gradient turbulent boundary layers using high-spatial-resolution particle image velocimetry. *Exp. Therm. Fluid Sci.* **129**, 110469.

Simens, M.P., Jiménez, J., Hoyas, S. & Mizuno, Y. 2009 A high-resolution code for turbulent boundary layers. *J. Comput. Phys.* **228** (11), 4218–4231.

Simonich, J.C. & Bradshaw, P. 1978 Effect of free-stream turbulence on heat transfer through a turbulent boundary layer. *Trans. ASME J. Heat Transfer* **100**, 671–677.

Smith, C.R. & Metzler, S.P. 1983 The characteristics of low-speed streaks in the near-wall region of a turbulent boundary layer. *J. Fluid Mech.* **129**, 27–54.

Smits, A.J., Matheson, N. & Joubert, P.N. 1983 Low-Reynolds-number turbulent boundary layers in zero and favorable pressure gradients. *J. Ship Res.* **27** (03), 147–157.

Spalart, P.R. 1988 Direct simulation of a turbulent boundary layer up to $Re_\theta = 1410$. *J. Fluid Mech.* **187**, 61–98.

Straub, S., Forooghi, P., Marocco, L., Wetzel, T., Vinuesa, R., Schlatter, P. & Frohnapfel, B. 2019 The influence of thermal boundary conditions on turbulent forced convection pipe flow at two Prandtl numbers. *Intl J. Heat Mass Transfer* **144**, 118601.

Subramanian, C.S. & Antonia, R.A. 1981 Effect of Reynolds number on a slightly heated turbulent boundary layer. *Intl J. Heat Mass Transfer* **24** (11), 1833–1846.

Tennekes, H. & Lumley, J.L. 1972 *A First Course in Turbulence*. MIT Press.

Tohdoh, K., Iwamoto, K. & Kawamura, H. 2008 Direct numerical simulation of passive scalar transport in a turbulent boundary layer. In *Proceedings of the 7th International ERCOFTAC Symposium on Engineering Turbulence Modelling and Measurements, Limassol, Cyprus* (ed. W. Rodi), pp. 169–174. ERCOFTAC.

VINUESA, R., HOSSEINI, S.M., HANIFI, A., HENNINGSON, D.S. & SCHLATTER, P. 2017 Pressure-gradient turbulent boundary layers developing around a wing section. *Flow Turbul. Combust.* **99** (3), 613–641.

VINUESA, R. & NAGIB, H.M. 2016 Enhancing the accuracy of measurement techniques in high Reynolds number turbulent boundary layers for more representative comparison to their canonical representations. *Eur. J. Mech. B/Fluids* **55**, 300–312.

VREMAN, A.W. & KUERTEN, J.G.M. 2014 Comparison of direct numerical simulation databases of turbulent channel flow at $Re_\tau = 180$. *Phys. Fluids* **26** (1), 015102.

WIKSTRÖM, P. 1998 Measurements, direct numerical simulation and modeling of passive scalar transport in turbulent flows. PhD thesis, KTH Royal Institute of Technology, Stockholm, Sweden.

WU, X. & MOIN, P. 2009 Direct numerical simulation of turbulence in a nominally zero-pressure-gradient flat-plate boundary layer. *J. Fluid Mech.* **630**, 5–41.